Published in final edited form as:
Cell. 2018 May 03; 173(4): 934–945.e12. doi:10.1016/j.cell.2018.02.062.

Visualization of membrane pore in live cells reveals a dynamic-pore theory governing fusion and endocytosis

Wonchul Shin[1], **Lihao Ge**[1], **Gianvito Arpino**[1], **Seth A. Villarreal**[1], **Edaeni Hamid**[1], **Huisheng Liu**[1,η], **Wei-Dong Zhao**[1,ϕ], **Peter J. Wen**[1], **Hsueh-Cheng Chiang**[1,ξ], and **Ling-Gang Wu**[1,*]

[1]National Institute of Neurological Disorders and Stroke, Bethesda, Maryland

Summary

Fusion is thought to open a pore to release vesicular cargoes vital for many biological processes, including exocytosis, intracellular trafficking, fertilization and viral entry. However, fusion pores have not been observed and thus proved in live cells. Its regulatory mechanisms and functions remain poorly understood. With super-resolution STED microscopy, we observed dynamic fusion pore behaviors in live (neuroendocrine) cells, including opening, expansion, constriction, and closure, where pore size may vary between 0 and 490 nm within 26 ms to seconds (vesicle size: 180–720 nm). These pore dynamics crucially determine the efficiency of vesicular cargo release and vesicle retrieval. They are generated by competition between pore expansion and constriction. Pharmacology and mutation experiments suggest that expansion and constriction are mediated by F-actin-dependent membrane tension and calcium/dynamin, respectively. These findings provide the missing live-cell evidence proving the fusion-pore hypothesis, and establish a live-cell dynamic-pore theory accounting for fusion, fission and their regulation.

Introduction

Fusion and fission, which mediate many biological processes, such as exocytosis, endocytosis, intracellular trafficking, cell division, fertilization, and viral entry, are thought to involve a membrane pore for releasing vesicular contents and for membrane scission (Lindau and Alvarez de Toledo, 2003; Chernomordik and Kozlov, 2008; Saheki and De Camilli, 2012; Alabi and Tsien, 2013; Wu et al., 2014; Antonny et al., 2016; Chang et al., 2017). Four lines of evidence collected in the last half a century support this view. First,

---

[*] Corresponding author and lead contact. wul@ninds.nih.gov.
[η] Current address: Beijing Advanced Innovation Center for Precision Medicine, Beihang University, Beijing, China
[ϕ] Current address: Department of Developmental Cell Biology, China Medical University, Shenyang, China
[ξ] Current address: Department of Pharmacology, College of Medicine, National Cheng Kung University, Tainan city, Taiwan

Author contributions: W.S. performed and analysed most experiments. L.G., E.H., H.L., W.D.Z. P.J.W., and H.C. C help performing STED imaging. G.A. and S.A.V. performed electron microscopic works. L.G.W. designed experiments and wrote the manuscript with helps from all authors. W.S. participated in designing experiments.

Declaration of interests: The authors declare no competing interests.

electron microscopy (EM) at synapses shows pore-like structures thought to reflect fusion or fission (Ceccarelli et al., 1973; Heuser and Reese, 1981; Miller and Heuser, 1984; Koenig and Ikeda, 1989; Shupliakov et al., 1997; Watanabe et al., 2013). However, EM is difficult to distinguish if the structure is for fusion, fission, on the way of expansion or closure, or formed by unknown mechanisms. Second, postsynaptic or amperometric current time course, which reflects transmitter release, diffusion, and postsynaptic or amperometric current generation, may imply fusion pore dynamics (Chow et al., 1992; Albillos et al., 1997; Wang et al., 2003; Alabi and Tsien, 2013; Li et al., 2016). Third, fluorescently tagged vesicular proteins, lipids or quantum dots loaded into vesicles are released with different kinetics, implying different fusion pore dynamics (Aravanis et al., 2003; Taraska et al., 2003; Zhang et al., 2009). Different sizes of fluorescent dyes can be differentially loaded into vesicles, implying different fusion or fission pore sizes (Takahashi et al., 2002; Vardjan et al., 2007). A vesicle-like cavity is sometimes observed after content release in PC12 cells, implying a fusion pore that does not collapse (Taraska et al., 2003). Fourth, conductance measurements may estimate <~5 nm fusion or fission pore for <~1 μm vesicles (Albillos et al., 1997; Klyachko and Jackson, 2002; He et al., 2006; He et al., 2009). However, this estimate assumes a cylindrical geometry with a constant length, solution conductance, and membrane conductance while pore size changes. These assumptions are not verified, and pores > ~5 nm are usually beyond the conductance measurement limit.

The above studies lead to a widely held view, called here as the metastable narrow-pore theory: fusion forms a narrow pore that either closes rapidly to limit the speed and the extent of releasing vesicular cargoes (kiss-and-run), or expands irreversibly till flattened (full-collapse) to promote release, and fission requires forming a narrow pore wrapped by dynamin or dynamin-like proteins for membrane scission (Lindau and Alvarez de Toledo, 2003; Saheki and De Camilli, 2012; Alabi and Tsien, 2013; Wu et al., 2014; Antonny et al., 2016; Chang et al., 2017). Pore regulation under this framework is thought to determine fusion and fission efficiency. However, fusion or fission pore has not been directly observed and thus proved in any live cells. Tools for direct pore observation in live cells are needed to prove the fusion/fission pore hypothesis, various hypothesized pore behaviors, underlying mechanisms and functions.

Recently, fusion-generated vesicular-shape profiles were observed with stimulated emission depletion (STED) microscopy in neuroendocrine cells containing ~300 nm vesicles (Zhao et al., 2016), raising the possibility of seeing fusion pore in live cells. However, the study did not examine or report fusion pore. Here, we performed STED imaging at ~60 nm resolution every 26–300 ms, which represents one of the highest spatiotemporal resolution for live-cell membrane structures (except single particle tracking and fluorescence correlation spectroscopy) (Lagerholm et al., 2017). We visualized fusion pore dynamics in live cells for the first time, providing the missing live-cell visualization evidence proving the existence of fusion and fission pore.

To our surprise, the metastable narrow-pore theory could not account for live-cell data. Instead, fusion instantly (<26 ms) or slowly opens a pore between 0 and 490 nm, which is two orders of magnitude wider than previously thought (<~5 nm), yet is metastable and does not flatten as full-collapse fusion. Neither expected is that these large pores can constrict and close instantly or slowly. Dynamic opening, expansion, constriction and closure of 0–490 nm pores determine fusion and fission efficiency – the rate of releasing contents and retrieving vesicles. Such dynamic behaviours reflect the net outcome of competition between pore expansion and constriction. Expansion involves actin-dependent membrane tension, whereas constriction involves calcium and dynamin, as suggested by pharmacology and mutation experiments. These findings establish a live-cell pore theory with extremely dynamic pore behaviours and novel underlying mechanisms and functions governing fusion and fission.

Results

Observing fusion pores in live cells

Bovine chromaffin cells were overexpressed with EGFP or mNeonGreen attached to phospholipase C delta PH domain (PH_G), which binds to PtdIns(4,5)P2 (PIP_2) at the plasma membrane (PM) cytosolic-facing leaflet and thus labels PM (Zhao et al., 2016). With Atto 532 (A532) in the bath, whole-cell 1-s depolarization (−80 to +10 mV, $depol_{1s}$, Figure 1A) induced calcium currents (ICa), capacitance changes reflecting exo-endocytosis (Figure 1B), and A532 spots surrounded by PH_G-labelled rings that reflected A532/PH_G diffusion from bath/PM to fusion-generated Ω-profiles (Figure 1C) (Zhao et al., 2016). While PH_G rings without A532 may appear due to hemi-fusion (Zhao et al., 2016), we focused on fusion pore and thus excluded hemi-fusion for analysis in this study, unless mentioned otherwise.

Images in Figure 1C were obtained at the XY plane with a fixed Z plane near cell bottom under the STED microscope (XY/Z_{fix} imaging). The PH_G-labelled ring diameter (346 ± 8 nm, 102 rings, 7 cells) was similar to the vesicle diameter (Albillos et al., 1997). We rescanned these structures at the STED XZ plane every 50 nm along Y-axis (XZ/Y_{stack} imaging, X, 12–15 µm; Z, 1–2 µm; Y, 1–5 µm; XY resolution, ~60 nm; Z resolution, ~150–200 nm; ~5–23 s/stack), confirming these structures as PH_G-labelled Ω-profiles (PH-Ω, Figure 1D). 25 ± 3% of PH-Ω (267 PH-Ω, 21 cells) showed visible pores (called $Pore_v$, Figures 1D, 1E and 1H-left). The remaining PH-Ω's pore was permeable to A532, but not visible (called $Pore_{noV}$, Figures 1F, 1G and 1H-right), because it was below the STED resolution (~60 nm).

The PH_G line profile across $Pore_v$ (Figure 1E), but not $Pore_{noV}$ (Figure 1G), was V-shape with a full-width-half-maximum (W_H) of 179 ± 12 nm (65–490 nm, 67 $Pore_v$, Figure 1I). Simulation shows that $Pore_v$ W_H faithfully reflects pore diameter when pore is larger than the STED resolution (Figure S1). XY-plane images, reconstructed from XZ/Y_{stack} images at the pore's Z-plane, showed an oval/round pore (W_H: 184 ± 12 nm, n = 67; Figures 1E) similar to corresponding XZ-plane $Pore_v$, confirming the observation of $Pore_v$. Expected from a pore's geometry, PH-Ω's neck and $Pore_v$ were filled with A532 with a similar shape at both the XZ- and XY-plane (Figures 1D, 1E and 1H-left).

As the PH-Ω diameter ranged from 180 to 720 nm (Figure 1I), $Pore_v$ W_H increased (Figure 1J), but the ratio between $Pore_v$ W_H and PH-Ω diameter ($Pore_v$/Ω) remained similar (mean: 41 ± 2%, 67 $Pore_v$, Figure 1K). We noticed large variation of $Pore_v$ W_H from near 0 up to the PH-Ω diameter at similar PH-Ω diameter (Figures 1J and 1K), which might reflect multiple mechanisms in controlling Pore_v (see results later).

Four additional sets of evidence further indicated Pore_v as the fusion pore. First, when mCLING-A488 (membrane-binding fluorophore-cysteine-lysine-palmitoyl group attached with Atto 488) was added in the bath (Revelo et al., 2014), it inserted into PM, diffused into, and thus labelled the fusion-generated Ω-profile together with overexpressed PH-mCherry (Zhao et al., 2016). Pore_v W_H measured from mCLING-A488 and PH-mCherry was similar (153 ± 6 nm vs 178 ± 5 nm, 8 pores/8 cells, Figure 2A), indicating that Pore_v is independent of PIP_2 detection.

Second, vesicles were loaded with fluorescent false neurotransmitter FFN511 via bath application (Figure 2B) (Gubernator et al., 2009). Depol_{1s} induced PH-Ω with Pore_v that released FFN511 (Figure 2C, n = 8), indicating Pore_v as the fusion pore for releasing FFN511. In cells overexpressed with NPY-mTurquoise2 (NPY-mT) inside granules and PH_G (Figure 2D), depol_{1s} induced PH-Ω with Pore_v that released NPY-mT (Figure 2E, n = 4), indicating Pore_v as the fusion pore for releasing vesicular contents. Third, EM revealed Ω-profiles with pores of 12–430 nm during KCl-induced depolarization (92 ± 12 nm, 53 pores, ~800 cell-cross-sections, Figure 2F and 2G), similar to the STED-measured Pore_v range. The diameter for pores >60 nm (152 ± 18 nm, 25 pores) was also similar to, and thus supported STED-measured Pore_v at ~60 nm resolution. All Ω-profiles did not contain a dense core (n = 53, Figure 2F and 2G), suggesting that the dense core is released via a pore narrower than the dense core. Fourth, rapid Pore_v opening described below indicates fusion pore opening.

Rapid fusion pore opening

To visualize pore dynamics, we performed STED XZ scanning of PH_G/A532 every 26–300 ms per frame with the Y-focal plane fixed (XZ/Y_fix scanning). In 1183 cells subjected to 1 depol_{1s} at the whole-cell configuration (1183 XZ/Y_fix scans), depol_{1s} induced 236 PH-Ω having a clear outline and containing a A532 spot (Figure 2H and 2I). We selected PH-Ω with a clear outline (Figure S2), because Pore_v was evident only at Y-focal planes with clear outline, as revealed by XZ/Y_stack imaging (Figure 1D).

Among 236 PH-Ω with clear outlines, 51 (49 cells) showed Pore_v (W_H: 142 ± 6 nm, Figures 2H, S3A). Pore_v was identified as having a V-shape PH_G fluorescence line profile, the amplitude of which was >3 times the standard deviation before fusion (Figure S3A). This large amplitude was not observed at Pore_noV (n = 185, Figures 2I, S3B) or without PH-Ωs (300 cells randomly selected, Figure S3C). Most (43/51) Pore_v was observed simultaneously with A532 spot at their first appearance, as imaged every 100–300 ms (n = 18), 46 ms (n = 21) or 26 ms (n = 4), indicating rapid fusion pore opening (Figures 2H, S3A). PH-Ω at 26–46 ms after fusion was much dimmer than at later times (Figures 2H, 3A), due to slow PH_G diffusion into the Ω-profile (see also Zhao et al., 2016).

Pore expansion, constriction, closure or unchanged

While most (43/51) Pore_v were observed at the fusion onset (Figures 2H, 3A), some (8/51) were observed at ~0.5–4 s after fusion (e.g., Figure 3B, summarized in 3F), suggesting slow pore expansion from a A532-permeable Pore$_{noV}$ to Pore$_{v}$. This was not due to movements along Y-axis, because during XY/Z$_{fix}$ imaging (Figure 1C), Ω-profiles did not move at the XY-plane (102 events, 7 cells, Figure S4A) (see also Chiang et al., 2014).

At the first frame Pore$_{v}$ was observed, Pore$_{v}$ reached the maximal size, which was less than the Ω-profile diameter (51 Pore$_{v}$, Figure 3A–3E). After Pore$_{v}$ appeared, it (51 pores, 49 cells) may change in four patterns (Figure 3F): 1) constriction till pore not visible (<60 nm), but permeable to A532 (17 pores, Figure 3A), 2) pore constriction and closure (impermeable to A532, 11 pores, Figure 3C), 3) maintaining a similar size (9 pores, Figure 3D), 4) disappearance (14 pores, Figure 3E, see Figure S4B for schematic drawing), due to rapid Ω-profile shrinking (Chiang et al., 2014; Wen et al., 2016) that precluded further analysis. We did not observe Pore$_{v}$ dilation till flattening.

After Pore$_{v}$ constricted and closed (Figure 3C), but not just constricted (Figure 3A), A532 spot fluorescence (excited strongly) decreased to baseline, due to pore closure that prevented bleached A532 (by strong excitation) from exchanging with bath fluorescent A532 (Chiang et al., 2014; Zhao et al., 2016). Similar A532 spot fluorescence decrease was observed when Pore$_{noV}$ closed (Figure S4C). The A532 fluorescence decrease is not due to a constricted pore smaller than A532 molecule size (~1.2 nm) (Erickson, 2009), because after the spot fluorescence decrease, bath application of an acid solution cannot quench the pH-sensitive VAMP2-EGFP or VAMP2-pHluorin overexpressed at the same spot, indicating that the spot is impermeable to smallest molecules like H^+ and OH^-, and thus is closed (Chiang et al., 2014; Zhao et al., 2016).

Pore expansion and constriction speed

Since Pore$_{v}$ reached the maximum at their first appearance as imaged every 26 ms, dividing Pore$_{v}$ W$_{H}$ by 26 ms yielded a pore expansion rate of >8.9 ± 1.0 nm/ms (n = 4, Figure 3A), the first direct measurement of the pore expansion rate. This represents the fastest rate, because delayed expansion (Figure 3B) was not included. With 26 ms resolution, the true value is underestimated. If within 26 ms, pores are first small, and then expand rapidly, as implicated in some pore conductance or amperometric measurements (Lindau and Alvarez de Toledo, 2003), it is beyond our detection resolution.

Pore$_{v}$ could constrict to <60 nm rapidly (<46–300 ms, 18 pores, Figures 3C and 5D) or slowly (1–20 s, 10 pores, Figure 3A). The fastest Pore$_{v}$ constriction was observed within one 46-ms frame from visible to non-visible, yielding a constriction rate of >3.3 ± 0.2 nm/ms (Figure 3C, n = 7). Pore constriction rate was not correlated with the preceding pore expansion rate (Figure S4D), suggesting that expansion and constriction are controlled by different mechanisms.

Mechanisms of constriction and expansion

Since calcium and dynamin trigger and mediate fusion pore closure (Chiang et al., 2014; Zhao et al., 2016), we wondered whether they constrict fusion pores. We first examined Pore$_{v}$ constriction within ~20 s after Pore$_{v}$ was observed, which should be minimally influenced by the initial pore expansion at the fusion onset. As the ICa density (ICa divided by the cell membrane capacitance) increased, the percentage of Pore$_{v}$ that subsequently constricted and/or closed (Constrict%, e.g., Figures 3A and 3C) increased significantly (Figure 4A), suggesting that high calcium influx facilitates constriction. Similarly, replacing bath calcium with strontium (Sr^{2+}) significantly reduced $Pore_v$ constrict% (Figure 4B and 4C, XZ/Y_{fix} imaging) and thus $Pore_v$ closure (see results later). Sr^{2+} also significantly increased the percentage of $depol_{1s}$-induced PH-Ω with a $Pore_v$ ($Pore_v$%), as detected with XZ/Y_{stack} imaging of PH_G/A532 every 5–23 s, during which $Pore_v$ should be converted to $Pore_{noV}$ if constriction occurs (Figure 4D and 4E). These results suggest that calcium influx facilitates $Pore_v$ constriction. Similarly, dynasore reduced $Pore_v$ constrict% (Figure 4B and 4C, XZ/Y_{fix} imaging); dynasore or overexpressed dynamin dominant-negative mutant, Dynamin 1-K44A, increased $Pore_v$% detected with XZ/Y_{stack} imaging every 5–23 s (Figure 4D and 4E), suggesting that dynamin may constrict $Pore_v$. $Depol_{1s}$-induced capacitance jumps were similar in control, dynasore, or overexpressed dynamin 1-K44A (Figure S5A), suggesting that dynamin does not play a major role in regulating release induced by $depol_{1s}$.

XZ/Y_{fix} imaging every 26–300 ms showed that Sr^{2+} and dynasore increased $Pore_v$% at the beginning of fusion (Figure 4F), suggesting that calcium/dynamin-dependent constriction may compete with initial pore expansion to control the pore size. Consistently, $Pore_v$% at the beginning of fusion decreased as the ICa density increased from ~26 to ~61 pA/pF in control cells (Figure 4G, XZ/Y_{fix}), suggesting that strong calcium influx facilitates constriction and thus may compete with pore expansion at the beginning of fusion. Interestingly, $Pore_v$% at the beginning of fusion was lower when the ICa density was very low, ~9 pA/pF (Figure 4G, bell-shape), supporting a role of calcium in pore expansion. It is likely that high calcium influx initiates strong constriction to overcome calcium-dependent initial pore expansion, resulting in $Pore_v$% reduction at higher ICa density (Figure 4G). While only one data point is consistent with calcium in pore expansion, multiple sets of data measured every 26–300 ms or 5–23 s at and after fusion onset in different ICa density or in Sr^{2+} (Figure 4A–G) suggest that high calcium influx facilitates pore constriction at and after fusion onset.

To determine whether membrane tension facilitates pore expansion (reviewed in Alabi and Tsien, 2013), we increased the bath osmolarity from 310 (control) to 650 mOsm, which decreases cell volume, reduces membrane tension, and inhibits Ω-profile shrinking in chromaffin cells (Boulant et al., 2011; Tsujita et al., 2015; Wen et al., 2016). Increased osmolarity reduced the $Pore_v$% from ~25–56% to ~13–16% in the presence of Ca^{2+} (bath), Sr^{2+}, or dynasore (Figure 4H, XZ/Y_{stack} imaging), and increased the $Pore_{noV}$ percentage correspondingly (Figure S5B). Thus, even with Sr^{2+} or dynasore to inhibit constriction (Figures 4B–4F), reducing membrane tension inhibited pore expansion (Figure 4H), suggesting that membrane tension is needed for pore expansion regardless of the presence of the constriction force or not. The increased osmolarity did not significantly affect $depol_{1s}$-induced capacitance jump (Figure S5C) or the hemi-fusion events (Figures S5D and S5E), suggesting that increased osmolarity does not significantly affect release induced by $depol_{1s}$.

Filamentous actin (F-actin) maintains PM tension (Boulant et al., 2011; Tsujita et al., 2015; Wen et al., 2016). In chromaffin cells, Latrunculin A (Lat A) disrupts F-actin polymerization, reduces membrane tension, and mimics the increased bath osmolarity (reducing membrane tension) in inhibiting shrink-fusion (for detail, see Wen et al., 2016). Lat A decreased the $Pore_v$% at the beginning of fusion in the absence or presence of Sr^{2+} or dynasore (Figure 4I, XZ/Y_{fix} imaging), suggesting that F-actin-dependent membrane tension is needed for pore expansion.

Taken together, these results (Figure 4A–I) suggest that calcium/dynamin-dependent pore constriction competes with F-actin/tension-dependent pore expansion, the net outcome of which generates various pore dynamics (Figure 4J). Further supporting this suggestion, dynamin 2-EGFP (or dynamin 1-EGFP) puncta were present at the PM, as labelled with A532 (Figure 4K) (Zhao et al., 2016), and were associated with most NPY-mT-labelled granules docked at the PM (108/144 granules, 12 cells, Figure 4K-left). Lifeact-TagGFP2-labelled F-actin was also associated with PM and docked NPY-mT-labelled granules (57/61 granules, 8 cells, Figure 4K-right) (Gabel et al., 2015; Wen et al., 2016). 1–5 dynamin 2-mTurquoise2 puncta surrounded PH_G-labelled $Pore_v$ induced by $depol_{1s}$ (32/32 $Pore_v$, 9 cells, Figure 4L, XZ/Y_{stack} imaging). Thus, dynamin may physically surround large $Pore_v$ for constriction.

Pore dynamics decide exo- and endocytosis efficiency

A532 and PH_G diffusion into PH-Ωs was much faster through $Pore_v$ than $Pore_{noV}$ (Figures 5A–5C). Similarly, for granules loaded with FFN511 (Figure 2B), FFN511 release through PH_G-labelled $Pore_v$ was ~12 times faster than through $Pore_{noV}$ (Figures 5D–5F). These results suggest that larger/faster pore expansion releases transmitters and exchanges contents/lipids more rapidly.

Inhibiting constriction with Sr^{2+} or dynasore increased the $Pore_v$% (Figure 4E and 4F), shortened the time of A532 and PH_G diffusion into Ω-profiles (Figure 5G), blocked fusion pore closure (Figures 5H), and inhibited capacitance-measured whole-cell endocytosis (Figure 5I). These results suggest that pore constriction limits vesicular cargo release and exchange with the bath solution, but serves as a prerequisite step for fusion pore closure and endocytosis.

Redefining kiss-and-run concept: pore size and release rate

$Pore_v$ closure (Figure 3C) predicts rapid/complete content release, in contrast to a popular notion that kiss-and-run mostly involves rapid closure of a narrow fusion pore to limit release (reviewed in Alabi and Tsien, 2013; Wu et al., 2014; Chang et al., 2017). To test this prediction, we performed confocal cell-bottom XY/Z_{fix} imaging of NPY-EGFP overexpressed in the vesicular lumen with Alexa 647 (A647) in the bath. We used confocal imaging, as STED was not needed and bleaching was less. $Depol_{1s}$ induced NPY-EGFP spot release, accompanied by sudden A647 spot appearance at the same location (Figure 6A–E, 218 spots, 28 cells), due to A647 diffusion into the fusion-generated Ω-profile (Chiang et al., 2014). A647 spots (under strong excitation) changed in three patterns (Chiang et al., 2014): 1) spot dimming while spot size remained unchanged, termed close-fusion (Ω-profile pore closure, Figure 6A), 2) persistent spot presence, termed stay-fusion (Ω-profile with an open pore, Figure 6B-left), and 3) spot shrinking till undetectable, termed shrink-fusion (Ω-profile shrinking and merging with PM, Figure 6B-right). Close-fusion (after closure) is impermeable not only to A647, but also to the smallest molecules like H^+ and OH^-; and the Ω-profile size may change before pore closure or during stay-fusion (Chiang et al., 2014).

Consistent with previous studies (Taraska et al., 2003; Perrais et al., 2004), NPY-EGFP spot release could be rapid (< 2 s, Figure 6A and 6B), slow (Figure 6C), partial or negligible (Figure 6D) (summarized in Figure 6E, 218 spots, 28 cells). NPY-EGFP release was sometimes preceded by a fluorescent increase (Figure 6C and 6D), due to pore opening that increased the vesicular lumen pH, and thus the pH-sensitive EGFP fluorescence (Taraska et al., 2003).

95% (90 out of 95) of close-fusion events detected with A647 imaging released NPY-EGFP completely and mostly rapidly (< 2 s) with a 20–80% decay time similar to non-close-fusion, which included stay- and shrink-fusion (Figures 6A, 6B and 6E). Thus, like non-close-fusion, most close-fusion involves a pore much larger than the ~4 nm EGFP molecule (Palm et al., 1997).

The remaining 5% close-fusions did not release NPY-EGFP, but was permeable to A647 before closure (Figures 6D-left and 6E). 9% (11/123) of non-close-fusions released NPY-EGFP slowly (6–12 s, Figures 6C and 6E), and 0.8% (1/123) of non-close-fusions partially released NPY-EGFP (Figures 6D-right, 6E). The slow or partial release of non-close-fusions was due to stay-fusion (Figures 6C and 6D-right). Thus, both close-fusion and non-close-fusion occasionally limited content release, consistent with studies showing small fusion pore conductance, and slow or partial release mostly at low frequencies (Alabi and Tsien, 2013; Wu et al., 2014). We concluded that close-fusion mostly involved a pore much larger than the 4 nm EGFP for rapid/complete release.

Close-fusion, which may open and close Pore_V within hundreds of milliseconds (Figure 3C) (Chiang et al., 2014), can approach the speed of ultrafast endocytosis, an endocytic form thought to take <~100 ms, but involves membrane invagination, large pit and bulk endosome formation at non-release sites of synapses (Watanabe et al., 2013). It is beyond the scope of the present work to determine whether ultrafast endocytosis occurs in our system.

Discussion

The fusion pore hypothesis has been accepted, but not proved with direct live-cell visualization. The metastable-narrow-pore theory is thought to govern fusion via a metastable narrow pore (<~5 nm) that either closes (kiss-and-run) or expand till flattened (full-collapse) (reviewed in Alabi and Tsien, 2013; Wu et al., 2014). Regulation of release is often attributed to regulation of kiss-and-run and full-collapse, thought to limit and facilitate release, respectively. By observing fusion-generated Ω-profiles with a pore that releases vesicular contents in live chromaffin cells (Figures 1–2, 5D), we provide the missing live-cell evidence proving the fusion-pore hypothesis. Our results establish a dynamic-pore theory (Figure 4J) that significantly advances over the narrow-pore theory, as detailed below.

We found that the metastable pore size range (0–490 nm, Figures 1–2) is two orders of magnitude wider than previously thought (<~5 nm). A large dynamic range of pores between 0 to 490 nm or between 0 and the vesicle width (Figures 1J and 1K) can expand, constrict, and/or close at various rates ranging from near 0 to >8.9 nm/s (Figure 3), resulting in diverse pore dynamics that generates diverse rates of content release and vesicle retrieval

(Figures 5–6). These dynamic pore behaviors result from competition between expansion and constriction, involving actin-dependent membrane tension and calcium/dynamin (Figure 4), respectively, to provide powerful expansion and constriction forces. The pore may disappear due to Ω-profile shrinking that merges the Ω-profile with the PM (Figure 3E) (Chiang et al., 2014; Wen et al., 2016). If the Ω-profile shrinks such that its depth is smaller than its pore, it literally becomes a full-collapse fusion (Figure S4B). This scenario, although beyond our detection limit to test, may reconcile the apparent difference between shrink-fusion and full-collapse fusion. These complex pore behaviours cannot be accounted for by the narrow-pore theory. We therefore suggest a dynamic-pore theory to account for our results and many years of published data interpreted under the narrow-pore theory. The dynamic-pore theory (Figure 4J) advances over the narrow-pore theory in three aspects. First, the metastable pore range increases from <~5 nm to <~490 nm or to the vesicle width, and it serves as the decision point not just for subsequent closure and collapse, but for expansion, constriction, closure, no change, and disappearance via Ω-profile shrinking (Figure S4B). Second, the release rate does not simply depend on narrow pore closure or full-collapse, but on competition between expansion and constriction that generates various sizes of pores at diverse rates. Third, F-actin-dependent tension and calcium/dynamin mediate expansion and constriction, respectively, as suggested from pharmacological and mutation experiments.

The dynamic-pore theory redefines kiss-and-run concept and how fusion pore controls release. Traditional kiss-and-run, which involves mostly rapid closure of a narrow pore to limit the extent and rate of release (Alabi and Tsien, 2013; Wu et al., 2014), is redefined as close-fusion, involving mostly large pores for rapid/complete release, but sometimes narrow pores to limit release (Figures 3C and 6). Kiss-and-run (close-fusion) is not the only fusion mode that can limit release. Non-kiss-and-run, particularly stay-fusion, may also limit release via a narrow pore (Figures 5 and 6). Consequently, decades of studies that interpret rapid/complete release, pores beyond conductance measurement resolution of ~3–5 nm, or release of ~20 nm quantum dots as full-collapse fusion, and otherwise as kiss-and-run, may be subject to errors (Albillos et al., 1997; Klyachko and Jackson, 2002; Taraska et al., 2003; Lindau and Alvarez de Toledo, 2003; He et al., 2006; Doreian et al., 2008; Zhang et al., 2009; Alabi and Tsien, 2013; Wu et al., 2014; Chang et al., 2017). With overwhelming observations of rapid/complete release and/or large pores attributed to full-collapse, kiss-and-run may be significantly underestimated, and thus may be more widespread than previously recognized. Supporting this possibility, kiss-and-run in chromaffin cells is a major endocytic mechanism (Chiang et al., 2014; Zhao et al., 2016). Pore conductance measurements reveal that kiss-and-run can involve a pore larger than the detection limit, ~3–5 nm, which may generate rapid/complete release in mast cells (Spruce et al., 1990), chromaffin cells (Ales et al., 1999), and calyx of Held nerve terminals (He et al., 2006). The volume occupied by the vesicle in PC12 cells may sometimes remain after releasing a large luminal protein, tissue plasminogen activator, implying kiss-and-run or stay-fusion with a large pore (Taraska et al., 2003).

Knowing that close-fusion does not necessarily limit content release, decades of studies that interpret different extents and rates of release as kiss-and-run and non-kiss-and-run fusion is no longer a safe practice. Based on the correlation between the directly measured pore size and the rate of FFN511 release or PH_G/A532 diffusion into fusing Ω-profiles (Figure 5), we suggest that diverse release rates and their regulation reported in previous studies reflect regulation of fusion pore dynamics under the dynamic-pore theory. Consistent with this suggestion, catecholamine release rate is correlated with the fusion pore conductance (Albillos et al., 1997; Ales et al., 1999). Different frequencies of nerve stimulation induce differential release of catecholamine and neuropeptides in chromaffin cells, implying that fusion pore dynamics may regulate release in physiological conditions (Fulop et al., 2005).

Compared to the narrow-pore theory where release is either limited by narrow pore closure or facilitated by full-collapse, the dynamic-pore theory offers more accurate control of content release by regulating pore size and expansion rate in a much larger dynamic range. Furthermore, the dynamic-pore theory decouples the control of release with endocytosis, whereas the narrow-pore theory links inhibition and facilitation of release to rapid kiss-and-run and classical endocytosis (following full-collapse), respectively. Thus, it is advantageous for cells to employ dynamic-pore mechanisms to control release and endocytosis independently and accurately.

Since $Pore_v$/Ω remained similar and did not exceed 100% in Ω-profiles ranging from 180 to 720 nm (Figure 1K), our results may apply to smaller vesicles. Indeed, even for ~30–40 nm Ω-profiles in neurons, pores as large as 5–40 nm were observed (Heuser and Reese, 1981; Watanabe et al., 2013; Wen et al., 2016). If our results apply to synapses containing 30–50 nm vesicles, release of ~20 nm quantum dot, which was attributed to full-collapse fusion (Zhang et al., 2009), could be mediated by kiss-and-run. Kiss-and-run at synapses might thus be more abundant than previously thought. Verifying this implication would be an important future research direction.

F-actin facilitates content release (Berberian et al., 2009) and dynamin limits release (Tsuboi et al., 2004; Trexler et al., 2016), implicating regulation of fusion pores by F-actin and dynamin (Tsuboi et al., 2004; Berberian et al., 2009; Trexler et al., 2016). Direct pore visualization combined with pharmacological manipulation and mutation suggests that F-actin provides membrane tension to expand the pore and dynamin constricts the pore (Figure 4). Dynamin was proposed to expand (Graham et al., 2002; Anantharam et al., 2011; Trexler et al., 2016) or stabilize the fusion pore (Holroyd et al., 2002; Tsuboi et al., 2004; Trexler et al., 2016), although neither proposal was supported by direct pore-dynamics evidence. Pore-dynamics imaging suggests that dynamin surrounds and constricts 65–490 nm pores, which counteracts pore-expansion (Figure 4). A new model may be needed to account for dynamin wrapping and constriction of such large pores, given that current models only account for ~5–20 nm narrow pores (Antonny et al., 2016).

Constricting the large pore of Ω-profiles or membrane invaginations is an essential endocytic step towards forming a narrow pore for fission, but poorly understood. Here we visualized constriction of 65–490 nm pores, showed the involvements of calcium/dynamin in constriction, and found that constriction is crucial in mediating endocytosis, closing fusion pores, and limiting cargo release (Figures 3–5). These findings may be of general significance, because calcium/dynamin-dependent pore constriction may contribute to mediate calcium/dynamin-dependent endocytosis, calcium/dynamin-dependent fusion pore closure, and dynamin-dependent receptor-mediated endocytosis widely observed in endocrine cells, neurons, and non-secretory cells (Saheki and De Camilli, 2012; Wu et al., 2014; Chiang et al., 2014; Antonny et al., 2016).

Calcium binding with synaptotagmins triggers fusion pore opening and facilitates initial fusion pore opening within ~5 nm, as detected with pore conductance measurements (Scepek et al., 1998; Segovia et al., 2010). Consistent with this finding, we observed an increase of $Pore_V$% (Figure 4G) as the ICa density increased from a very low value to a medium level, at which constriction force was not maximal (Figure 4A). It is likely that calcium may facilitate both expansion and constriction, but favouring expansion and constriction at low and high ICa, respectively. Calcium sensors, such as calmodulin and synaptotagmin 1, which are involved in endocytosis (reviewed in Wu et al., 2014), are candidates for mediating calcium-dependent constriction.

The technique and theory presented here provide an imaging tool and new theoretical foundation to study pore dynamics of many processes, such as exocytosis, endocytosis, intracellular trafficking, fertilization, and viral entry. Although our STED resolution is ~60 nm, pore resolution may reach ~40 nm, because PH_G was attached to the PM cytosolic leaflet, which was the pore membrane outer leaflet (see Methods for detail). With ~40–60 nm resolution per 26–300 ms, we could not examine 0–40 nm fusion pore within milliseconds of fusion, during which small-molecule transmitters are often released (Chang et al., 2017). Improving spatiotemporal resolution is crucial to overcome this problem in the future.

In summary, we visualize fusion and fission pore dynamics in live cells and establish a dynamic-pore theory with novel pore dynamics, underlying mechanisms and key functions accounting for fusion, endocytosis and their regulations. We redefine the kiss-and-run concept and suggest reinterpreting release and fusion pore data in previous studies with the dynamic-pore theory. Our results suggest calcium and dynamin in mediating large-pore constriction, which is essential for endocytosis, fusion pore closure, and for counteracting F-actin/tension-dependent pore expansion. These findings may be of widespread applicability, given that pore dynamics mediate many biological processes, including exocytosis, endocytosis, intracellular trafficking, cell-cell or organelle-organelle fusion/division, fertilization, and viral entry.

STAR*METHODS

KEY RESOURCES TABLE

REAGENT or RESOURCE	SOURCE	IDENTIFIER
Chemicals, Peptides, and Recombinant Proteins		
DMEM medium	Gibco	Cat#11885092
Fetal bovine serum	Gibco	Cat#10082147
Poly-L-lysine	Sigma	P4832; CAS: 25988-63-0
Laminin	Sigma	L2020; CAS: 114956-81-9

REAGENT or RESOURCE	SOURCE	IDENTIFIER
Atto 532	Sigma	88793
Alexa 647	Sigma	A20502
Trypsin inhibitor	Sigma	T9253; CAS: 9035-81-8
Bovine serum albumin	Sigma	A2153; CAS: 9048-46-8
mCLING-Atto 488	Synaptic Systems	Cat#710 006AT3
FFN511	Abcam	Cat#ab120331
Embed-812	EMS	Cat#13940
Collagenase P	Sigma	COLLP-RO Roche 11249002001
Dynasore	Tocris Bioscience	Cat#2897; CAS: 30448-55-3
Latrunculin A	Tocris Bioscience	Cat#3973; CAS: 76343-93-6
Critical Commercial Assays		
Basic Primary Neurons Nucleofector Kit	Lonza	Cat#VVPI-1003
Experimental Models: Primary Cell Culture		
Bovine adrenal chromaffin cell	J. W. Treuth and Sons, Inc.	Adrenal Glands
Recombinant DNA		
PH-EGFP	Várnai P. and Balla T. 1998	Addgene Plasmid #51407
PH-mCherry	Chisari et al., 2009	Addgene Plasmid #36075
mNeonGreen	Allele Biotechnology	ABP-FP-MNEONSB
PH-mNeonGreen	This paper	N/A
NPY-EGFP	Taraska et al., 2003	Addgene Plasmid #74629
Dynamin 2-EGFP	He K. et al., 2015	Addgene Plasmid #34686
mTurquoise2	Goedhard et al., 2012	Addgene Plasmid #54843
NPY-mTurquoise2	This paper	N/A
Dynamin 2-mTurquoise2	This paper	N/A
Dynamin 1-K44A-mRFP	Hynes et al., 2004	Addgene Plasmid #55795
Lifeact-TagGFP2	Ibidi	Cat#60112
Software and Algorithms		
Huygens Professional	Scientific Volume Imaging	https://svi.nl/Huygens-Professional
Image J	NIH	https://imagej.nih.gov/ij/
LAS X	Leica	https://www.leicabiosystems.com/
Igor Pro	WaveMetrics	http://www.wavemetrics.com/

CONTACT FOR REAGENT AND RESOURCE SHARING

Further information and requests for resources and reagents should be directed to and will be fulfilled by the Lead Contact, Ling-Gang Wu, at wul@ninds.nih.gov

EXPERIMENTAL MODEL AND SUBJECT DETAILS

Primary cell culture—Fresh adult (21 – 27 months old) male bovine adrenal glands purchased from a local abattoir (J. W. Treuth and Sons, Inc.) were used to prepare primary chromaffin cell culture, which are widely used for the study of exo- and endocytosis (Lindau and Alvarez de Toledo, 2003; Wu et al., 2014).

METHOD DETAILS

Chromaffin cell culture—We prepared primary bovine adrenal chromaffin cell culture as described previously (Chiang et al., 2014). Fresh adult (21 – 27 months old) bovine adrenal glands (from a local abattoir) were immersed in pre-chilled Lock's buffer on ice containing: NaCl, 145 mM; KCl, 5.4 mM; Na2HPO4, 2.2 mM; NaH2PO4, 0.9 mM; glucose, 5.6 mM; HEPES, 10 mM (pH 7.3, adjusted with NaOH). Glands were perfused with Lock's buffer, then infused with Lock's buffer containing collagenase P (1.5 mg/ml, Roche), trypsin inhibitor (0.325 mg/ml, Sigma) and bovine serum albumin (5 mg/ml, Sigma), and incubated at 37°C for 20 min. The digested medulla was minced in Lock's buffer, and filtered through a 100 μm nylon mesh. The filtrate was centrifuged (48 × g, 5 min), re-suspended in Lock's buffer and re-centrifuged until the supernatant was clear. The final cell pellet was re-suspended in pre-warmed DMEM medium (Gibco) supplemented with 10% fetal bovine serum (Gibco).

Electroporation and plating—Cells were transfected by electroporation using Basic Primary Neurons Nucleofector Kit (Lonza), according to the manufacturer's protocol and plated onto poly-L-lysine (0.005 % w/v, Sigma) and laminin (4 μg/ml, Sigma) coated glass coverslips. The cells were incubated at 37°C with 9% CO2 and used within 5 days.

Plasmids and fluorescent dyes—The PH-EGFP (phospholipase C delta PH domain attached with EGFP) was obtained from Dr. Tamas Balla. NPY-EGFP and PH-mCherry were purchased from Addgene. Lifeact-TagGFP2 was purchased from Abidi (Germany). NPY-mTurquoise2 (NPY-mT) construct was created by replacing the EGFP tag of NPY-EGFP with mTurquoise2 (Addgene). PH-mNeonGreen construct was created by replacing the EGFP tag of PH-EGFP with mNeonGreen (Allele Biotechnology) (Shaner et al., 2013). Both PH-EGFP and PH-mNeonGreen are abbreviated as PH_G. Dynamin 2-mTurquoise2 construct was created by replacing the EGFP tag of dynamin 2-EGFP (Addgene) with mTurquoise2 (Addgene). Dynamin 1-K44A-mRFP was purchased from Addgene.

For imaging, the dye concentration in the bath solution was: Atto 532 (A532, Sigma), 30 μM; Alexa 647 (A647, Sigma), 30 μM. For experiments using membrane-binding fluorophore-cysteine-lysine-palmitoyl group attached with Atto 488 (mCLING-A488, Synaptic Systems), before imaging was performed, 0.5 μM mCLING-A488 was added into the bath solution for 10 min and then washed out. For FFN511 (Abcam) imaging, cells were bathed with FFN511 (5–10 μM) for 3 min and images were performed after washing out FFN511 in the bath solution.

Overexpression of PH_G or NPY-EGFP did not significantly affect the basic properties of exo- and endocytosis, because 1) whole-cell capacitance measurements and imaging show robust exo- and endocytosis, and similar percentages of close-fusion and non-close-fusion as control (Chiang et al., 2014; Zhao et al., 2016), and 2) Ω-profile's pore could also be resolved by imaging extracellularly applied mCLING-A488 or by EM (Figure 2).

Electrophysiology—At room temperature (20 – 22°C), whole-cell voltage-clamp and capacitance recordings were performed with an EPC-10 amplifier together with the software lock-in amplifier (PULSE, HEKA, Lambrecht, Germany) (Lindau and Neher, 1988; Chiang et al., 2014). The holding potential was −80 mV. For capacitance measurements, the frequency of the sinusoidal stimulus was 1000 – 1500 Hz with a peak-to-peak voltage ≤ 50 mV. The bath solution contained 125 mM NaCl, 10 mM glucose, 10 mM HEPES, 5 mM $CaCl_2$, 1 mM $MgCl_2$, 4.5 mM KCl, 0.001 mM TTX and 20 mM TEA, pH 7.3 adjusted with NaOH. The pipette (2 – 4 MΩ) solution contained 130 mM Cs-glutamate, 0.5 mM Cs-EGTA, 12 mM NaCl, 30 mM HEPES, 1 mM $MgCl_2$, 2 mM ATP, and 0.5 mM GTP, pH 7.2 adjusted with CsOH. These solutions pharmacologically isolated calcium currents.

For stimulation, we used a 1-s depolarization from the holding potential of −80 mV to +10 mV ($depol_{1s}$). We used this stimulus, because it induces robust exo-endocytosis as reflected in capacitance recordings (Figure 1B) (Engisch and Nowycky, 1998; Perrais et al., 2004; Chiang et al., 2014).

STED imaging—STED images were acquired with Leica TCS SP8 STED 3× microscope that is equipped with a 100 × 1.4 NA HC PL APO CS2 oil immersion objective and operated with the LAS-X imaging software. Excitation was with a tunable white light laser and emission was detected with hybrid detectors. In time-gated STED mode, PH-EGFP and A532 were sequentially excited at 470 and 532 nm, respectively, with the 592 nm STED depletion beam, and their fluorescence collected at 475–525 nm and 540–587 nm, respectively. PH-mNeonGreen and A532 were sequentially excited at 485 and 540 nm, respectively, with the 592 nm STED depletion beam, and their fluorescence collected at 490–530 nm and 545–587 nm, respectively.

mCLING-A488 and PH-mCherry were sequentially excited at 488 and 570 nm, respectively, with the 660 nm STED depletion beam, and their fluorescence collected at 504–555 nm and 575–650 nm, respectively.

For three-color STED imaging with 592 nm STED depletion laser, dynamin 2-EGFP (or Lifeact-TagGFP2), NPY-mT, and A532 were excited at 488 nm, 442 nm, and 540 nm, respectively, and their fluorescence collected at 493–535 nm, 447–482 nm, and 545–587 nm, respectively. PH-mNeonGreen and FFN511 (or dynamin 2-mTurquoise2 or NPY-mTurquoise2) were sequentially excited at 505 and 442 nm, respectively, with the 592 nm STED depletion beam, and their fluorescence collected at 510–587 nm and 447–490 nm, respectively.

The excitation power for A532 was 10% of the maximum, at which fluorescent A532 can be bleached within a few seconds. This feature was used to distinguish whether the fusion pore is closed or not, because pore closure prevents bleached A532 (caused by strong excitation) from exchange with fluorescent A532 in the bath, resulting in A532 spot fluorescence decay (Chiang et al., 2014). In contrast, an open pore would not cause A532 spot fluorescence decay, because an open pore allows for continuous exchange of bleached A532 in the Ω-profile with fluorescent A532 in the bath (Chiang et al., 2014).

STED imaging generally causes more photobleaching and phototoxicity. Severe phototoxicity could cause loss of the whole-cell giga seal during patch-clamp recording (Chiang et al., 2014). We avoided severe phototoxicity by applying only one $depol_{1s}$ and imaging for only ~30–40 s per cell. With this setting, we have not noticed significant differences in the exo- and endocytosis properties obtained under confocal and STED imaging conditions (Chiang et al., 2014; Zhao et al., 2016). For imaging of PH_G and A532, continuous exchange of bleached PH_G or A532 with fluorescent ones from non-imaging areas lessened the photobleaching problem.

STED scanning modes—STED images were acquired at the cell bottom with the XY (parallel to the coverslip) or XZ (perpendicular to the coverslip) scanning mode (Figure 1A). For XY/Z_{fix} scanning (Z focal plane was fixed at ~100–200 nm above the cell bottom), images were acquired every 200–300 ms at 15 nm per pixel in an XY area of ~10–15 µm × ~10–15 µm (Figure 1C). Most experiments were performed at the XZ/Y_{fix} scanning mode at the cell bottom, at which images were acquired every 26–300 ms at 15 nm per pixel in an XZ area of 19.4 µm × 0.7–1.5 µm, with a fixed Y-axis location (e.g., Figure 3). We used 300 ms per XZ frame at the beginning of this project, but used 46–100 ms as we realized the importance of catching fast events with fast imaging rates. Sometimes, we used 26 ms per XZ frame to determine the maximal rate of pore expansion. To reconstruct 3-D structure of fusion-generated Ω-profiles, XZ images (X-axis, 12–15 µm; Z-axis, 1–2 µm) were also acquired alone Y-axis every 50 nm for 1–5 µm (XZ/Y_{stack} scanning, collected within ~5–23 s).

The STED resolution for imaging PH_G (PH-EGFP or PH-mNeonGreen) in our conditions was ~60 nm on the microscopic X- and Y-axis (parallel to cell-bottom membrane or coverslip), and ~150–200 nm on the microscopic Z-axis. The probability of observing a PH-Ω-profile with clear outline during a XZ/Y_{fix} scan after $depol_{1s}$ was ~0.2 (observing 236 Ω-profiles from 1183 XZ/Y_{fix} scans after $depol_{1s}$). STED images were deconvolved using Huygens software (Scientific Volume Imaging).

STED pore closure identification—During XZ/Y_{fix} imaging, A532 was excited at a high laser power so that fluorescent A532 can be bleached with a time constant of 1.5–3.5 s. Pore closure was identified as the gradual dimming of the A532 spot fluorescence to baseline during XZ/Y_{fix} PH_G/A532 imaging. Figure 3C shows an example for $Pore_v$ constriction and closure, and Figure S4C shows an example for $Pore_{noV}$ closure. A532 fluorescence dimming is due to pore closure that prevents bleached A532 (by strong excitation) from exchange with a large reservoir of fluorescent A532 (very small molecule, ~1.2 nm) in the bath. This is not due to a narrow pore smaller than A532 molecule size, because after spot dimming, bath application of an acid solution cannot quench the pH-sensitive VAMP2-EGFP or VAMP2-pHluorin overexpressed at the same spot, indicating that the spot is impermeable to H^+ or OH^-, the smallest molecules, and thus is closed (Chiang et al., 2014; Zhao et al., 2016). Furthermore, the closure time course calculated from spot dimming matches approximately with whole-cell endocytosis time course (Chiang et al., 2014), and inhibition of dynamin by dynamin inhibitors, dynamin dominant-negative mutant dynamin 1-K44A, or dynamin knockdown blocks not only whole-cell endocytosis but also pore closure detected with the spot dimming method (Chiang et al., 2014; Zhao et al., 2016). These results further confirm that spot dimming under strong excitation reflects pore closure.

Confocal image acquisition—Imaging with A647 and NPY-EGFP were performed with an inverted confocal microscope (TCS SP5II, Leica, Germany, 100× oil objective, numerical aperture: 1.4), where A647 (30 μM in bath, Sigma) and NPY-EGFP were excited by a Diode laser at 640 nm (maximum power: 40 mW) and an Argon laser at 488 nm (maximum power: 50 mW), respectively. The 640 nm laser was set at 50% of the maximum power, which could bleach A647 inside the Ω-profile within a few seconds once the Ω-profile closed (Chiang et al., 2014). The 488 nm laser was set at 1.5 – 2% to avoid significant bleaching of NPY-EGFP. A647 fluorescence was collected with a photomultiplier at 650 – 720 nm, whereas NPY-EGFP, at 498 – 580 nm. Both excitation and fluorescence collection were done simultaneously at the XY/Z_{fix} scanning mode at the cell bottom. Confocal imaging area was ~70 – 160 μm^2 at the XY plane with a fixed Z-axis focal plane ~100–200 nm above the cell-bottom membrane. Images were collected every 10–33 ms at 50 – 70 nm per pixel at the XY/Z_{fix} scanning mode.

Fusion mode identification during confocal imaging—During confocal imaging of A647 (strong excitation, 50% maximal power) and NPY-EGFP (weak excitation: 1.5–2% maximal power) at the cell-bottom, we identified fusion modes based on A647 imaging as characterized in detail in our recent study (for detail, see Ref. (Chiang et al., 2014)). In brief, close-fusion was identified if after A647 spot appeared, the spot A647 fluorescence intensity (F_{647}) decayed to baseline with a time constant more than 2 s (~2–5 s) while the spot W_H did not change. Another form of fusion, the Ω-shrink fusion, in which the fusion-generated Ω-profile shrinks until undetectable, could also cause F_{647} decay to baseline (Chiang et al., 2014). However, this differs from Ω-profile pore closure in two aspects. First, the decay time constant of most Ω-shrink events is < 1.7 s (e.g., Figure 6B) (Chiang et al., 2014). Thus, a decay time constant of > 2 s is a safe criterion for identifying fusion pore closure (Chiang et al., 2014). Second, Ω-shrink fusion is accompanied by a reduction of A647 spot W_H, whereas close-fusion is not (Figure 6A and 6B) (Chiang et al., 2014). These two criteria allowed us to clearly identify close-fusion from shrink-fusion. For stay-fusion, A647 spot persisted, and F_{647} did not decay to baseline during our recording time of ~30 s.

Electron microscopy—Bovine chromaffin cells were stimulated for 90 s using a solution containing 70 mM KCl, 60 mM NaCl, 10 mM glucose, 10 mM HEPES, 2 mM $CaCl_2$, and 1 mM $MgCl_2$ (pH 7.3, adjusted with NaOH). The cells were then immediately fixed with 2% glutaraldehyde, 2% paraformaldehyde and 4% tannic acid in 0.1 M cacodylate buffer pH 7.4 for 15 min, followed by the same fixative without tannic acid for additional 15 min. The cells were washed first with a solution of 100 mM glycine in 0.1 M sodium cacodylate buffer for 1 min at room temperature, and then with just 0.1 M sodium cacodylate. After, post fixation with 1% OsO_4 for 1 hour on ice, the samples were then gradually dehydrated with increasing pure solutions of ethanol (50%, 70%), staining with 2% Uranyl acetate in 70% of ethanol for 30 min and continuing with dehydration (85%, 95%, 100%). Lastly, infiltration and embedding with Embed-812. The embedded samples were sectioned on an ultramicrotome with thicknesses of 70–90 nm. The resulting sections were placed on 200 mesh pioloform coated index grid. Single images were collected at up to 73,000X magnification on a JEOL JEM-200CX, 120kV electron microscope with an AMT XR-100 CCD.

Simulation—Simulation (in Figure S1) was done in Igor Pro (WaveMetrics).

QUANTIFICATION AND STATISTICAL ANALYSIS

Data selection—For every cell recorded with a pipette under the whole-cell configuration, the data within the first 2 min at the whole-cell configuration were used, which avoided rundown of endocytosis (gradual disappearance of endocytosis) as previously reported under the whole-cell configuration for a long time (Smith and Neher, 1997; Chiang et al., 2014). Cells expressed with PH_G (or PH-mCherry) were used for examining pore dynamics. The criteria for selecting PH-Ωs for pore analysis during XZ/Y_{fix} scanning are described in Figure S2 and its legends. Visible pores of PH-Ω-profiles ($Pore_v$) containing A532 at the XZ frame are identified based on two criteria: 1) the Ω-profile pore is visible as judged by eyes and A532 spot is inside the Ω-profile, and 2) the F_{PH} line profile across the pore region shows a V-shape valley with an amplitude at least three times larger than the standard deviation of the same F_{PH} line profile before fusion (e.g., Figure S3). The V-shape valley amplitude of the F_{PH} line profile was measured as shown in Figure S3A (see ‘Amp’ in Figure S3A).

For STED XZ/Y_{stack} analysis of fusion percentages and confocal image analysis of close-fusion and non-close fusion, cells with less than 5 fusion events were not used, which avoided large fluctuations from individual cells and thus improved the accuracy of the percentage measurement.

STED image analysis and pore measurements—STED images were analyzed with ImageJ and LAS X (Leica). While Ω-profiles labelled with PH, but filled with no A532 may appear due to hemi-fusion (Zhao et al., 2016), we only analysed Ω-profiles labelled with PH and filled with A532 throughout the work, except those shown in Figures S5D and S5E.

Pores labelled with PH_G, PH-mCherry, or mCLING-A488 at the XZ plane were identified based on the image and the fluorescence intensity line profile. We first identified the fluorescently labelled Ω-profiles with an open pore, the edge of which was continuous with the plasma membrane (e.g., Figures 1D, 1E, 2H and 3). As judged from the intensity line profile, the fluorescence intensity on the edge of the pore was usually higher than the plasma membrane (e.g., Figure 1D, 1E), due to a denser membrane area and thus more PH_G molecules within our STED resolution limit (XY: 60 nm; Z: 150–200 nm) (see simulation data in Figure S1). The intensity line profile in the pore region should show a valley with a peak at least three times larger than the baseline fluctuation (standard deviation) in the non-pore region (for detail, see Figure S3A–3C). The full-width-half-maximum (W_H) of the valley of the intensity line profile across the pore was proportional to the pore diameter, as shown with simulation (Figure S1). Thus, pore W_H faithfully reflects pore diameter.

During XZ/Y_{fix} scanning, some $depol_{1s}$-induced PH-Ω-profiles were out of the Y_{fix} focal plane, as the outline of the Ω-profile was vague or unclear (e.g., Figure S2B). These out-of-focus Ω-profiles were not included for analysis. The criteria for the selection of the Ω-profile are described in detail in Figure S2 and its legend.

STED pore resolution—Although our STED resolution is ~60 nm, the resolution on the pore diameter may reach ~40 nm, because the pore diameter measured from PH_G attached to PM_c (cytosolic leaflet, pore outer leaflet) was longer than the actual pore diameter (measured from the inner membrane leaflet) by ~20 nm. The 20 nm value was approximately equal to 2 times the distance between PM_c and PM_e (PM extracellular leaflet), which was 7.3 ± 0.1 nm (electron microscopic estimate, n = 20 cells, Figure S6), plus the ~4 nm EGFP molecule size (Palm et al., 1997). Supporting this estimate, the PH-mCherry-labelled pore W_H was 26 ± 2 nm larger than the pore W_H labelled with mCLING-A488 that binds to PM_e, the pore membrane inner leaflet (n = 8, paired t-test, $p<0.01$, Figure 2A).

Confocal image analysis—Confocal images were analyzed with ImageJ and LAS X (Leica). The fluorescence intensity from an area covering the fluorescence spot was measured at every image frame. The full-width-half-maximum (W_H) was measured from intensity profiles of 1 – 4 lines across the spot center.

Fusion-generated Ω-profiles may change in seven patterns, which are grouped into three categories: 1) the Ω-profile is maintained while its size may remain unchanged, enlarge, or shrink to some extent, termed stay-fusion, 2) the stay fusion is followed by pore closure, termed close-fusion, and 3) the Ω-profile shrinks until undetectable, leading to Ω-profile merging with the plasma membrane, termed shrink-fusion (for detail, see Chiang et al., 2014).

Statistical tests—Data were expressed as mean ± s.e.m. Replicates are indicated in results and figure legends. N represents the number of cells, pores, or Ω-profiles as indicated in results and figure legends. The statistical test used is *t* test or ANOVA. Although the statistics were performed based on the number of cells, pores, and Ω-profiles, each group of data were replicated from at least four primary chromaffin cell cultures. Each culture was from at least two glands from one bovine.

In several experimental groups, PH-Ω number was around or slightly more than 10. However, the statistical test was highly significant. Furthermore, our conclusions did not rely on a single statistical test, but on statistical tests in multiple conditions that consolidate our conclusions. For example, both Figure 4E and 4F show that Sr^{2+} and dynasore increased $Pore_v$%; reduction of $Pore_v$% by the increased osmolarity was repeatedly shown in the presence of calcium, Sr^{2+}, or dynasore (Figure 4H); reduction of $Pore_v$% by Lat A was repeatedly shown in the presence of calcium, Sr^{2+}, or dynasore (Figure 4I). In 123 non-close-fusion events, only one released NPY-EGFP partially (Figure 6E), indicating the rareness of partial release from non-close-fusion. However, we observed 11 non-close-fusion events that released NPY-EGFP very slowly (time constant: 6–12 s, Figure 6E). Thus, the rare partial release seems an extension of very slow release. Furthermore, partial release is consistent with the observation of fusion without releasing vesicular contents (Taraska et al., 2003).

Supplementary Material

Refer to Web version on PubMed Central for supplementary material.

Acknowledgments

This work was supported by NINDS Research Program (ZIA-NS003009-13). Gianvito Arpino is in the Karolinska Institutet-NIH Doctoral Partnership Program in Neuroscience. We thank Susan Cheng, Virginia Crocker and Oleg Shupliakov for EM technical support. We thank Uri Ashery for helpful comments on the manuscript.

References

Alabi AA, Tsien RW. Perspectives on kiss-and-run: role in exocytosis, endocytosis, and neurotransmission. Annu Rev Physiol. 2013; 75:393–422. [PubMed: 23245563]

Albillos A, Dernick G, Horstmann H, Almers W, Alvarez de Toledo G, Lindau M. The exocytotic event in chromaffin cells revealed by patch amperometry. Nature. 1997; 389:509–512. [PubMed: 9333242]

Ales E, Tabares L, Poyato JM, Valero V, Lindau M, Alvarez de Toledo G. High calcium concentrations shift the mode of exocytosis to the kiss-and-run mechanism. Nat Cell Biol. 1999; 1:40–44. [PubMed: 10559862]

Anantharam A, Bittner MA, Aikman RL, Stuenkel EL, Schmid SL, Axelrod D, Holz RW. A new role for the dynamin GTPase in the regulation of fusion pore expansion. Mol Biol Cell. 2011; 22:1907–1918. [PubMed: 21460182]

Antonny B, Burd C, De Camilli P, Chen E, Daumke O, Faelber K, Ford M, Frolov VA, Frost A, Hinshaw JE, Kirchhausen T, Kozlov MM, Lenz M, Low HH, McMahon H, Merrifield C, Pollard TD, Robinson PJ, Roux A, Schmid S. Membrane fission by dynamin: what we know and what we need to know. EMBO J. 2016; 35:2270–2284. [PubMed: 27670760]

Aravanis AM, Pyle JL, Tsien RW. Single synaptic vesicles fusing transiently and successively without loss of identity. Nature. 2003; 423:643–647. [PubMed: 12789339]

Berberian K, Torres AJ, Fang Q, Kisler K, Lindau M. F-actin and myosin II accelerate catecholamine release from chromaffin granules. J Neurosci. 2009; 29:863–870. [PubMed: 19158310]

Boulant S, Kural C, Zeeh JC, Ubelmann F, Kirchhausen T. Actin dynamics counteract membrane tension during clathrin-mediated endocytosis. Nat Cell Biol. 2011; 13:1124–1131. [PubMed: 21841790]

Ceccarelli B, Hurlbut WP, Mauro A. Turnover of transmitter and synaptic vesicles at the frog neuromuscular junction. J Cell Biol. 1973; 57:499–524. [PubMed: 4348791]

Chang CW, Chiang CW, Jackson MB. Fusion pores and their control of neurotransmitter and hormone release. J Gen Physiol. 2017; 149:301–322. [PubMed: 28167663]

Chernomordik LV, Kozlov MM. Mechanics of membrane fusion. Nat Struct Mol Biol. 2008; 15:675–683. [PubMed: 18596814]

Chiang HC, Shin W, Zhao WD, Hamid E, Sheng J, Baydyuk M, Wen PJ, Jin A, Momboisse F, Wu LG. Post-fusion structural changes and their roles in exocytosis and endocytosis of dense-core vesicles. Nat Commun. 2014; 5:3356. [PubMed: 24561832]

Chow RH, von Ruden L, Neher E. Delay in vesicle fusion revealed by electrochemical monitoring of single secretory events in adrenal chromaffin cells. Nature. 1992; 356:60–63. [PubMed: 1538782]

Doreian BW, Fulop TG, Smith CB. Myosin II activation and actin reorganization regulate the mode of quantal exocytosis in mouse adrenal chromaffin cells. J Neurosci. 2008; 28:4470–4478. [PubMed: 18434525]

Engisch KL, Nowycky MC. Compensatory and excess retrieval: two types of endocytosis following single step depolarizations in bovine adrenal chromaffin cells. J Physiol. 1998; 506(Pt 3):591–608. [PubMed: 9503324]

Erickson HP. Size and shape of protein molecules at the nanometer level determined by sedimentation, gel filtration, and electron microscopy. Biol Proced Online. 2009; 11:32–51. [PubMed: 19495910]

Fulop T, Radabaugh S, Smith C. Activity-dependent differential transmitter release in mouse adrenal chromaffin cells. J Neurosci. 2005; 25:7324–7332. [PubMed: 16093382]

Gabel M, Delavoie F, Demais V, Royer C, Bailly Y, Vitale N, Bader MF, Chasserot-Golaz S. Annexin A2-dependent actin bundling promotes secretory granule docking to the plasma membrane and exocytosis. J Cell Biol. 2015; 210:785–800. [PubMed: 26323692]

Graham ME, O'Callaghan DW, McMahon HT, Burgoyne RD. Dynamin-dependent and dynamin-independent processes contribute to the regulation of single vesicle release kinetics and quantal size. Proceedings of the National Academy of Sciences of the United States of America. 2002; 99:7124–7129. [PubMed: 11997474]

Gubernator NG, Zhang H, Staal RG, Mosharov EV, Pereira DB, Yue M, Balsanek V, Vadola PA, Mukherjee B, Edwards RH, Sulzer D, Sames D. Fluorescent false neurotransmitters visualize dopamine release from individual presynaptic terminals. Science. 2009; 324:1441–1444. [PubMed: 19423778]

He L, Wu XS, Mohan R, Wu LG. Two modes of fusion pore opening revealed by cell-attached recordings at a synapse. Nature. 2006; 444:102–105. [PubMed: 17065984]

He L, Xue L, Xu J, McNeil BD, Bai L, Melicoff E, Adachi R, Wu LG. Compound vesicle fusion increases quantal size and potentiates synaptic transmission. Nature. 2009; 459:93–97. [PubMed: 19279571]

Heuser JE, Reese TS. Structural changes after transmitter release at the frog neuromuscular junction. J Cell Biol. 1981; 88:564–580. [PubMed: 6260814]

Holroyd P, Lang T, Wenzel D, De Camilli P, Jahn R. Imaging direct, dynamin-dependent recapture of fusing secretory granules on plasma membrane lawns from PC12 cells. Proc Natl Acad Sci U S A. 2002; 99:16806–16811. [PubMed: 12486251]

Klyachko VA, Jackson MB. Capacitance steps and fusion pores of small and large-dense-core vesicles in nerve terminals. Nature. 2002; 418:89–92. [PubMed: 12097912]

Koenig JH, Ikeda K. Disappearance and reformation of synaptic vesicle membrane upon transmitter release observed under reversible blockage of membrane retrieval. J Neurosci. 1989; 9:3844–3860. [PubMed: 2573698]

Lagerholm BC, Andrade DM, Clausen MP, Eggeling C. Convergence of lateral dynamic measurements in the plasma membrane of live cells from single particle tracking and STED-FCS. J Phys D Appl Phys. 2017; 50:063001. [PubMed: 28458397]

Li X, Dunevall J, Ewing AG. Quantitative Chemical Measurements of Vesicular Transmitters with Electrochemical Cytometry. Acc Chem Res. 2016; 49:2347–2354. [PubMed: 27622924]

Lindau M, Alvarez de Toledo G. The fusion pore. Biochim Biophys Acta. 2003; 164:167–173.

Lindau M, Neher E. Patch-clamp techniques for time-resolved capacitance measurements in single cells. Pflugers Arch. 1988; 411:137–146. [PubMed: 3357753]

Miller TM, Heuser JE. Endocytosis of synaptic vesicle membrane at the frog neuromuscular junction. J Cell Biol. 1984; 98:685–698. [PubMed: 6607255]

Palm GJ, Zdanov A, Gaitanaris GA, Stauber R, Pavlakis GN, Wlodawer A. The structural basis for spectral variations in green fluorescent protein. Nat Struct Biol. 1997; 4:361–365. [PubMed: 9145105]

Perrais D, Kleppe IC, Taraska JW, Almers W. Recapture after exocytosis causes differential retention of protein in granules of bovine chromaffin cells. J Physiol. 2004; 560:413–428. [PubMed: 15297569]

Revelo NH, Kamin D, Truckenbrodt S, Wong AB, Reuter-Jessen K, Reisinger E, Moser T, Rizzoli SO. A new probe for super-resolution imaging of membranes elucidates trafficking pathways. J Cell Biol. 2014; 205:591–606. [PubMed: 24862576]

Saheki Y, De Camilli P. Synaptic vesicle endocytosis. Cold Spring Harb Perspect Biol. 2012; 4:a005645. [PubMed: 22763746]

Scepek S, Coorssen JR, Lindau M. Fusion pore expansion in horse eosinophils is modulated by Ca2+ and protein kinase C via distinct mechanisms. EMBO J. 1998; 17:4340–4345. [PubMed: 9687502]

Segovia M, Ales E, Montes MA, Bonifas I, Jemal I, Lindau M, Maximov A, Sudhof TC, Alvarez de TG. Push-and-pull regulation of the fusion pore by synaptotagmin-7. Proc Natl Acad Sci U S A. 2010; 107:19032–19037. [PubMed: 20956309]

Shaner NC, Lambert GG, Chammas A, Ni Y, Cranfill PJ, Baird MA, Sell BR, Allen JR, Day RN, Israelsson M, Davidson MW, Wang J. A bright monomeric green fluorescent protein derived from Branchiostoma lanceolatum. Nat Methods. 2013; 10:407–409. [PubMed: 23524392]

Shupliakov O, Low P, Grabs D, Gad H, Chen H, David C, Takei K, De Camilli P, Brodin L. Synaptic vesicle endocytosis impaired by disruption of dynamin-SH3 domain interactions. Science. 1997; 276:259–263. [PubMed: 9092476]

Spruce AE, Breckenridge LJ, Lee AK, Almers W. Properties of the fusion pore that forms during exocytosis of a mast cell secretory vesicle. Neuron. 1990; 4:643–654. [PubMed: 2344404]

Takahashi N, Kishimoto T, Nemoto T, Kadowaki T, Kasai H. Fusion pore dynamics and insulin granule exocytosis in the pancreatic islet. Science. 2002; 297:1349–1352. [PubMed: 12193788]

Taraska JW, Perrais D, Ohara-Imaizumi M, Nagamatsu S, Almers W. Secretory granules are recaptured largely intact after stimulated exocytosis in cultured endocrine cells. Proc Natl Acad Sci U S A. 2003; 100:2070–2075. [PubMed: 12538853]

Trexler AJ, Sochacki KA, Taraska JW. Imaging the recruitment and loss of proteins and lipids at single sites of calcium-triggered exocytosis. Mol Biol Cell. 2016; 27:2423–2434. [PubMed: 27307587]

Tsuboi T, McMahon HT, Rutter GA. Mechanisms of dense core vesicle recapture following “kiss and run” (“cavicapture”) exocytosis in insulin-secreting cells. J Biol Chem. 2004; 279:47115–47124. [PubMed: 15331588]

Tsujita K, Takenawa T, Itoh T. Feedback regulation between plasma membrane tension and membrane-bending proteins organizes cell polarity during leading edge formation. Nat Cell Biol. 2015; 17:749–758. [PubMed: 25938814]

Vardjan N, Stenovec M, Jorgacevski J, Kreft M, Zorec R. Subnanometer fusion pores in spontaneous exocytosis of peptidergic vesicles. J Neurosci. 2007; 27:4737–4746. [PubMed: 17460086]

Wang CT, Lu JC, Bai J, Chang PY, Martin TF, Chapman ER, Jackson MB. Different domains of synaptotagmin control the choice between kiss-and-run and full fusion. Nature. 2003; 424:943–947. [PubMed: 12931189]

Watanabe S, Rost BR, Camacho-Perez M, Davis MW, Sohl-Kielczynski B, Rosenmund C, Jorgensen EM. Ultrafast endocytosis at mouse hippocampal synapses. Nature. 2013; 504:242–247. [PubMed: 24305055]

Wen PJ, Grenklo S, Arpino G, Tan X, Liao HS, Heureaux J, Peng SY, Chiang HC, Hamid E, Zhao WD, Shin W, Nareoja T, Evergren E, Jin Y, Karlsson R, Ebert SN, Jin A, Liu AP, Shupliakov O, Wu LG. Actin dynamics provides membrane tension to merge fusing vesicles into the plasma membrane. Nat Commun. 2016; 7:12604. [PubMed: 27576662]

Wu LG, Hamid E, Shin W, Chiang HC. Exocytosis and endocytosis: modes, functions, and coupling mechanisms. Annu Rev Physiol. 2014; 76:301–331. [PubMed: 24274740]

Zhang Q, Li Y, Tsien RW. The dynamic control of kiss-and-run and vesicular reuse probed with single nanoparticles. Science. 2009; 323:1448–1453. [PubMed: 19213879]

Zhao WD, Hamid E, Shin W, Wen PJ, Krystofiak ES, Villarreal SA, Chiang HC, Kachar B, Wu LG. Hemi-fused structure mediates and controls fusion and fission in live cells. Nature. 2016; 534:548–552. [PubMed: 27309816]

Highlights

- Visualizing 0–490 nm pore opening, expansion, constriction and closure in live cell
- Competition between expansion and constriction generates diverse pore dynamics
- Actin/tension expands the pore and calcium/dynamin constricts up to 490 nm pore
- Establishing a dynamic-pore theory controlling fusion and fission efficiency

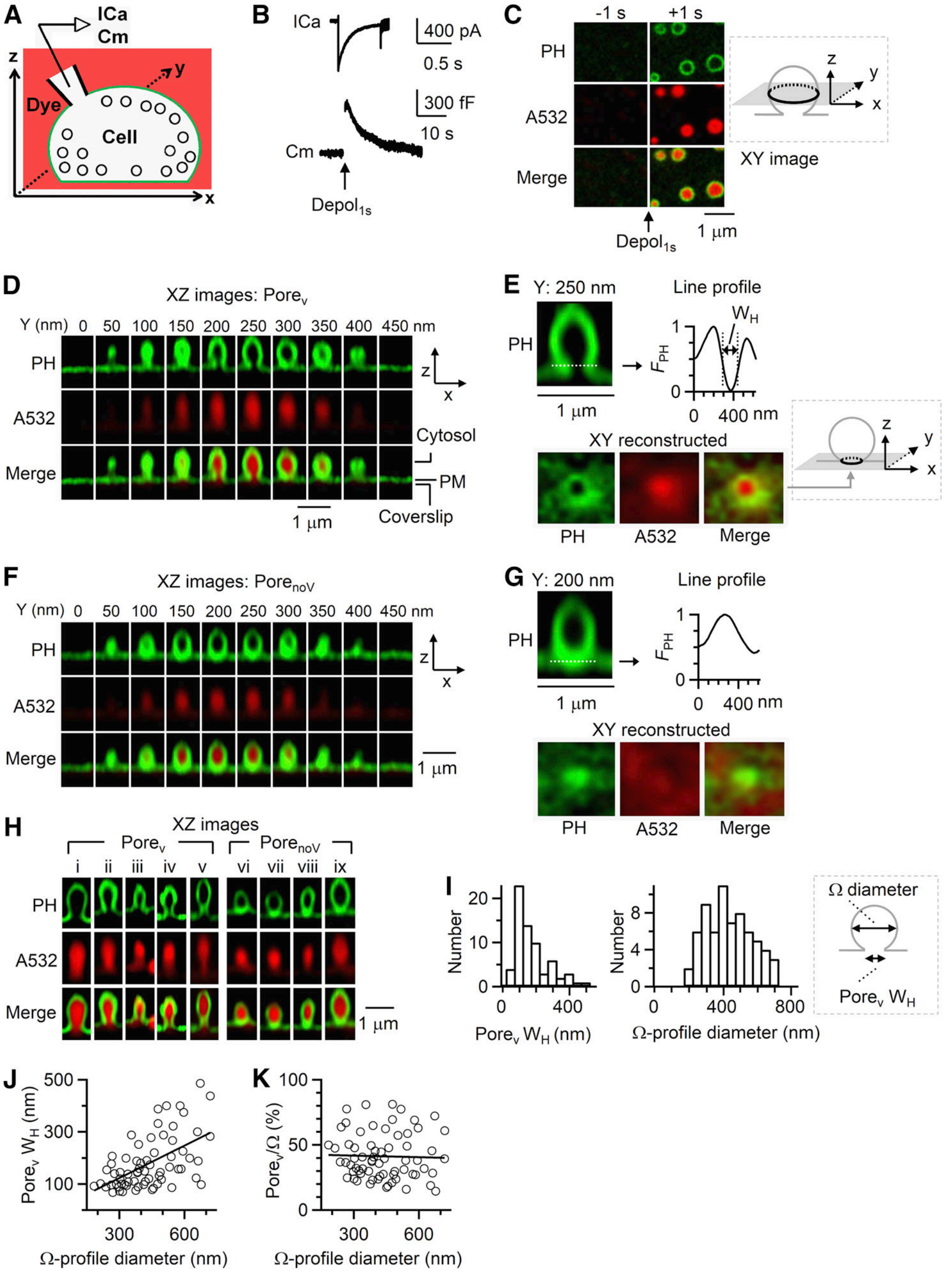

Figure 1. Ω-profiles with a pore in live cells

(A) Setup drawing. cell's membrane and bath are labelled with PH_G (green) and A532 (red, pseudo-color). ICa and Cm (capacitance) are recorded via a whole-cell pipette.

(B) ICa and Cm changes induced by $depol_{1s}$.

(C) STED XY/Z_{fix} images of PH_G and A532 before (−1 s) and after (+1 s) $depol_{1s}$. Inset: drawing of XY- focal plane, ~100–200 nm above cell-bottom.

(D) XZ PH_G/A532 images of a PH-Ω along Y-axis every 50 nm ($Pore_V$ observed). Cytosol, PM and coverslip location are labelled. XZ images are STED images (applies to Figures 1–5).

(E) Upper, PH-Ω at Y=250 nm from panel D and the fluorescence profile of the dotted line across the pore with W_H labelled.

Lower, XY images with a Z-focal plane at the pore (dotted line in upper panel). Images were reconstructed from panel D XZ/Y_{stack} images (inset: drawing of reconstructed plane in gray).

(F–G) Similar to panel D–E, respectively, but for a PH-Ω with $Pore_{noV}$.

(H) Sampled $depol_{1s}$-induced PH_G/A532-labelled Ω-profiles with $Pore_v$ (left: i–v) or $Pore_{noV}$ (right, vi–ix).

(I) Distribution of $Pore_v$ W_H and corresponding PH-Ω diameter (n = 67, binning width: 50 nm). Inset: drawing of $Pore_v$ W_H and PH-Ω diameter.

(J–K) $Pore_v$ W_H (J) and $Pore_v$/Ω ($Pore_v$ W_H/PH-Ω diameter, K) plotted versus PH-Ω diameter (n = 67, XZ/Y_{stack} imaging). Linear-fit correlation coefficient is 0.55 (J) and −0.03 (K); ANOVA test of linear fit: $p < 0.001$ (J), $p = 0.81$ (K).

See also Figure S1.

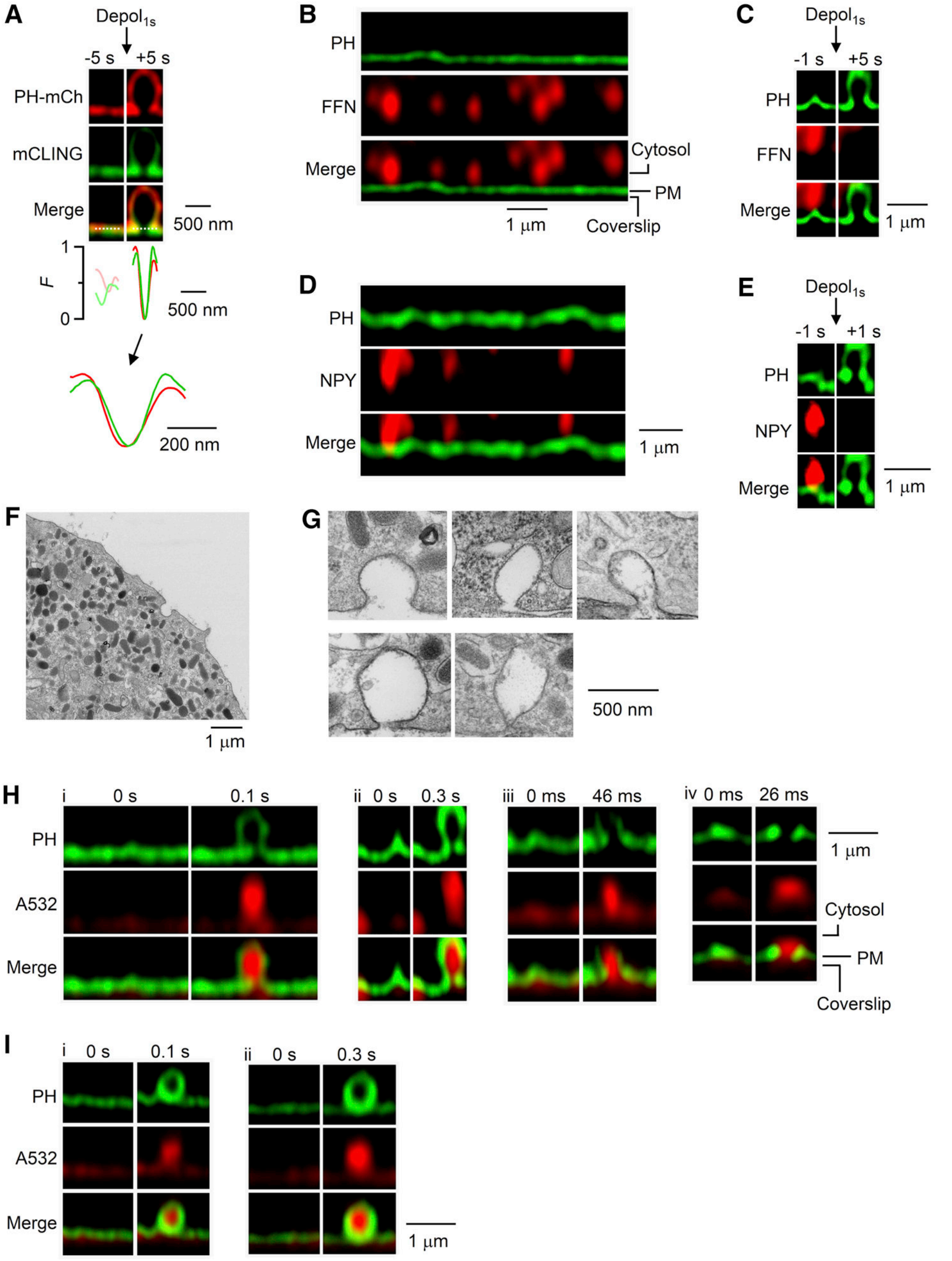

Figure 2. Observing rapid fusion pore opening and release

(A) PH-mCherry (PH-mCh, red) and mCLING-A488 (green) images and their fluorescence profile (F) across the dotted line (the pore) before (−5 s) and after (+5 s) depol$_{1s}$. F traces are also enlarged (Lower). Line profiles are normalized to the peak value after depol$_{1s}$. The cell was overexpressed with PH-mCh and treated with mCLING-A488 (0.5 μM, bath, 10 min).

(B) PH$_G$/FFN511 images at rest (pseudo-color). FFN511 was in the bath for 3 min, and then washed.

(C) PH$_G$/FFN511 images before (−1 s) and after (+5 s) depol$_{1s}$.

(D) PH$_G$/NPY-mT images at rest (pseudo-color).

(E) PH$_G$/NPY-mT images before (−1 s) and after (+1 s) depol$_{1s}$.

(F–G) EM images of a cell (F) and sampled Ω-profiles with different pore sizes (G). Cells were in 70 mM KCl for 90 s.

(H) Sampled PH_G/A532 images immediately before (time 0) and after fusion during XZ/Y_{fix} imaging every 0.1 s (i), 0.3 s (ii), 46 ms (iii), or 26 ms (iv). PH-Ω with a $Pore_v$ was induced by $depol_{1s}$ applied 0.1–2 s earlier.

(I) Similar to panel H, but showing $Pore_{noV}$ sampled every 0.1 s (i) or 0.3 s (ii).

See also Figures S2, S3 and S6.

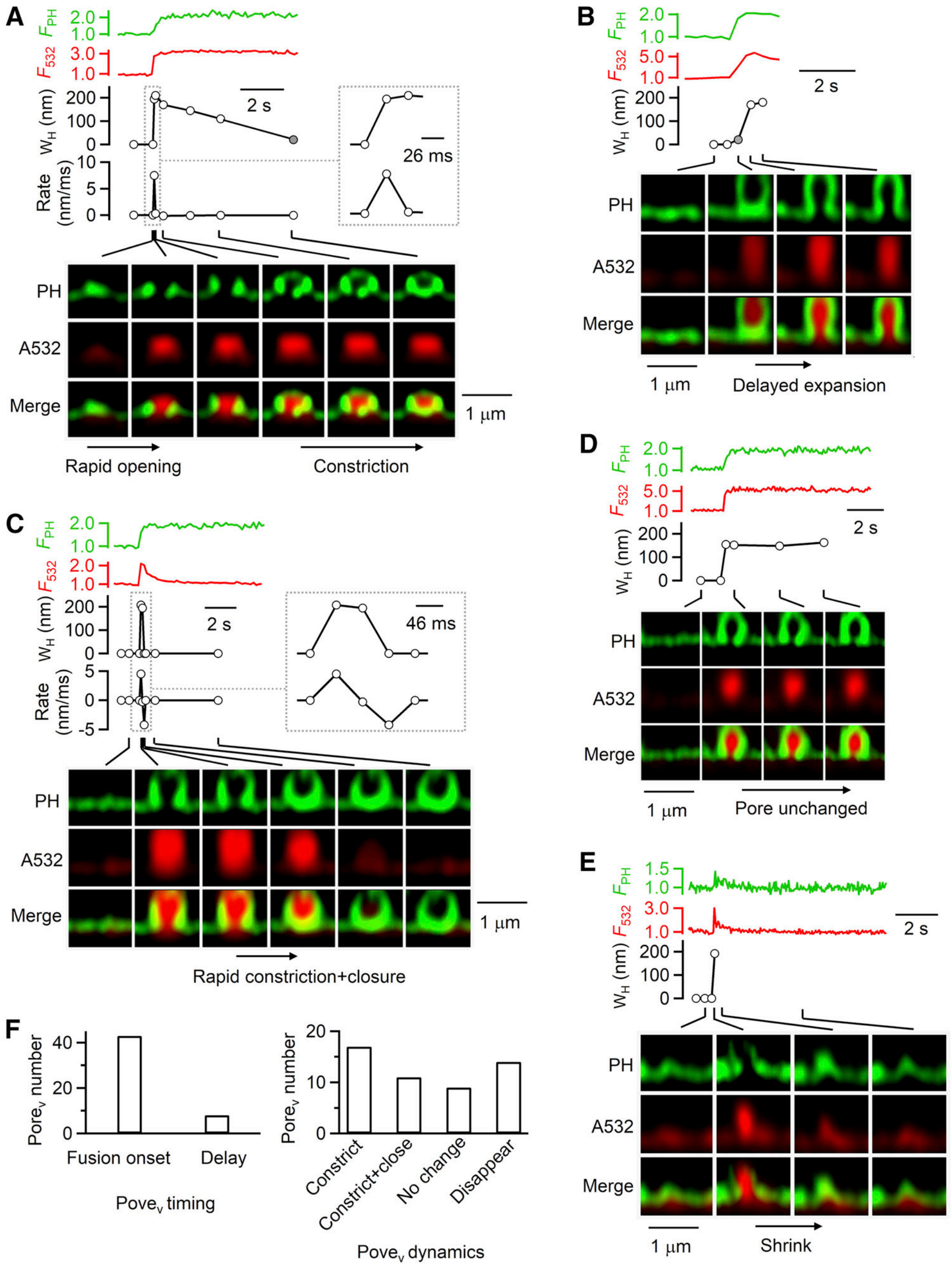

Figure 3. Fusion pore expansion, constriction and closure at different rates

(A–E) PH-Ω fluorescence (F_{PH}, normalized to baseline), A532 spot fluorescence (F_{532}, normalized to baseline), $Pore_v$ W_H, and sampled images at times indicated with lines showing different $Pore_v$ dynamics: A, rapid opening and slow constriction (same PH-Ω as in Figure 2H-iv); B, delayed expansion; C, rapid constriction and closure; D, $Pore_v$ unchanged; E, $Pore_v$ disappearance due to Ω-profile shrinking.

A and C: the rate of $Pore_v$ W_H changes (Rate) are plotted (A, 26 ms/frame; C, 46 ms/frame); insets, W_H and Rate at larger time scale. Gray circles in A–B refer to non-visible A532-

permeable pores with a W_H <60 nm. Fusion was induced by $depol_{1s}$ at 0.1–2 s before PH-Ω appeared.

(F) Left, number of $Pore_v$ observed at the fusion onset or 0.5–4 s after fusion (delay). Right, number of $Pore_v$ that subsequently constricted, constricted and closed, remained unchanged, or disappeared. Data from 51 $Pore_v$ (49 cells, XZ/Y_{fix} image every 26–300 ms). See also Figures S2 and S4.

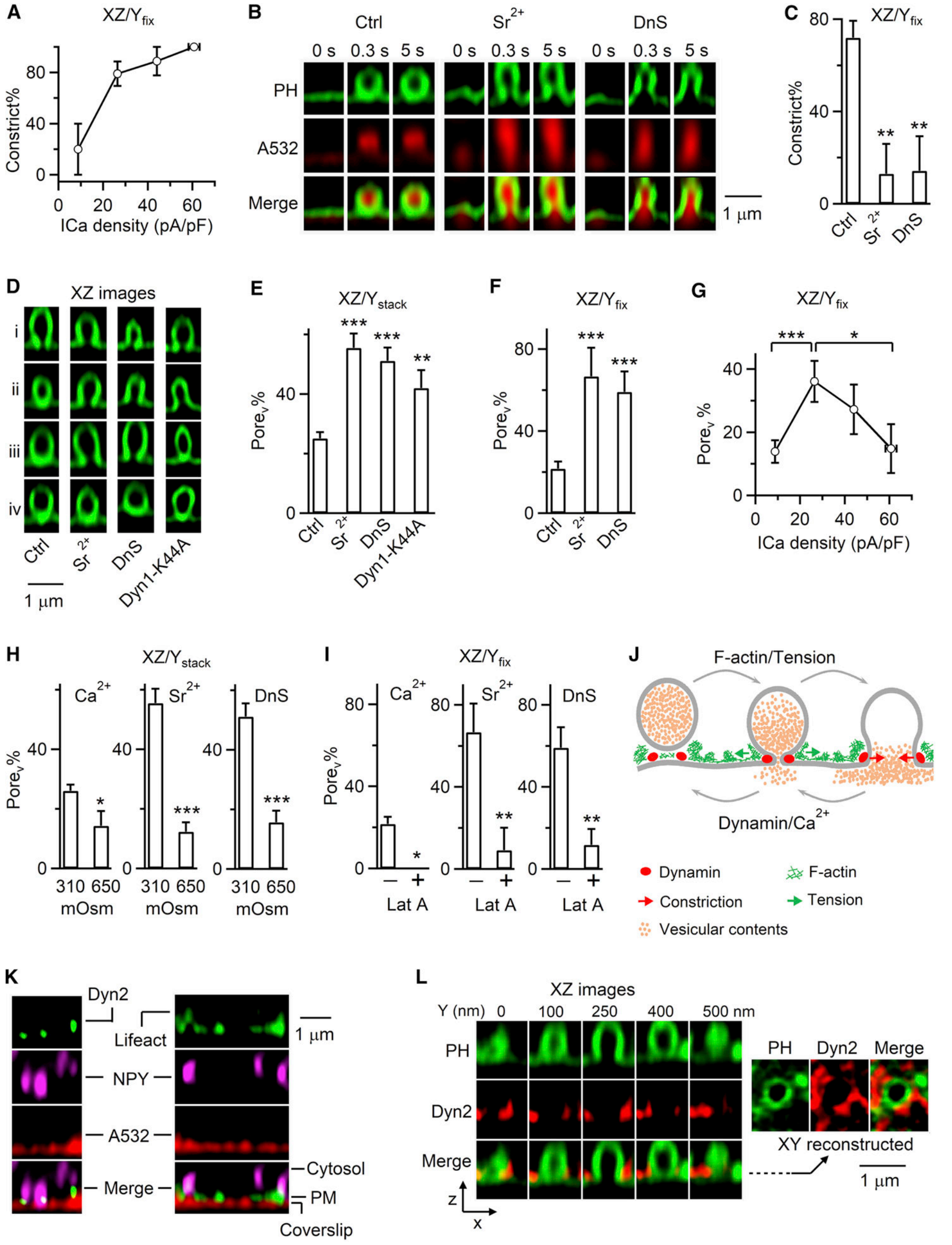

Figure 4. Mechanisms of pore constriction, expansion and their competition

(A) Percentage of Pore$_V$ undergoing constriction within 20 s after fusion (Constrict%, mean ± s.e.m.) is plotted versus ICa density (mean ± s.e.m.) of four cell groups with ICa density <15 pA/pF, 15–35 pA/pF, 35–50 pA/pF, and >50 pA/pF in control conditions (35 cells, 37 Pore$_V$). Pore$_V$ closure was counted as constriction; Ω-profiles undergoing shrinking were excluded, because shrinking obscured Pore$_V$ detection (also applies to C). Fusion was induced by depol$_{1s}$ (applies to all figures). P<0.01, ANOVA test.

(B) Sampled PH$_G$/A532 images before and after fusion in Ctrl, in the presence of Sr^{2+} (5 mM/bath, replacing Ca^{2+}) or dynasore (DnS, 80 μM/bath, XZ/Y$_{fix}$ imaging).

(C)Constrict% of Pore$_v$ in control (35 cells, 37 Pore$_v$), Sr^{2+} (7 cells, 8 Pore$_v$) or DnS (12 cells, 13 Pore$_v$). *, $P<0.05$; **, $P<0.01$; ***, $P<0.001$ (t test, compared to control, applies to all bar graphs).

(D–E) Sampled PH-Ω (D) and the percentage of PH-Ω with a Pore$_v$ (Pore$_v$%, E, mean + s.e.m.) in control (Ctrl, 21 cells, 267 PH-Ω), Sr^{2+} (5 mM, replacing bath Ca^{2+}, 8 cells, 119 PH-Ω), dynasore (DnS, 80 μM/bath, 7 cells, 88 PH-Ω), or overexpressed dynamin 1-K44A (7 cells, 81 PH-Ω). Pore$_v$ was detected with XZ/Y$_{stack}$ imaging every 5–23 s.

(F) Pore$_v$% at the beginning of fusion in control (202 cells, 236 PH-Ω), Sr^{2+} (10 cells, 12 PH-Ωs) or dynasore (DnS, 19 cells, 22 PH-Ωs). Pore$_v$ was detected with XZ/Y$_{fix}$ imaging every 26–300 ms.

(G) Pore$_v$% (mean ± s.e.m.) at the beginning of fusion plotted versus ICa density (mean ± s.e.m.) in four groups with different ICa densities described in panel A (202 cells, 236 PH-Ω). *, $P<0.05$; ***, $P<0.001$; t test. Pore$_v$ was detected with XZ/Y$_{fix}$ imaging.

(H) Pore$_v$% at 310 or 650 mOsm in Ca^{2+} (21 cells/267 PH-Ω or 7 cells/42 PH-Ω), Sr^{2+} (8 cells/119 PH-Ω or 13 cells/85 PH-Ω), or DnS (with 5 mM Ca^{2+}; 7 cells/88 PH-Ω or 7 cells/64 PH-Ω). Pore$_v$ was detected with XZ/Y$_{stack}$ imaging.

(I) Pore$_v$% at the beginning of fusion in the absence (−) or presence (+) of 3 μM Lat A in a bath containing Ca^{2+} (202 cells/236 Ω or 13 cells/15 PH-Ω), Sr^{2+} (10 cells/12 PH-Ω or 9 cells/11 PH-Ω) or DnS (10 cells/12 PH-Ω or 14 cells/17 PH-Ω). Pore$_v$ was detected with XZ/Y$_{fix}$ imaging.

(J) Model: F-actin/tension-dependent pore expansion competes with calcium/dynamin-dependent pore constriction to determine pore dynamics.

(K) Left, dynamin 2-EGFP (Dyn2), NPY-mT (granules) and A532 (bath) images. Right, lifeact-TagGFP2, NPY-mT and A532 images.

(L) Left, PH$_G$ and dynamin 2-mTurquoise2 (Dyn2) XZ-images at 10 s after depol$_{1s}$ (XZ/Y$_{stack}$ with Y-axis labelled).

Right, XY-reconstructed images across the pore (dotted line).

See also Figure S5.

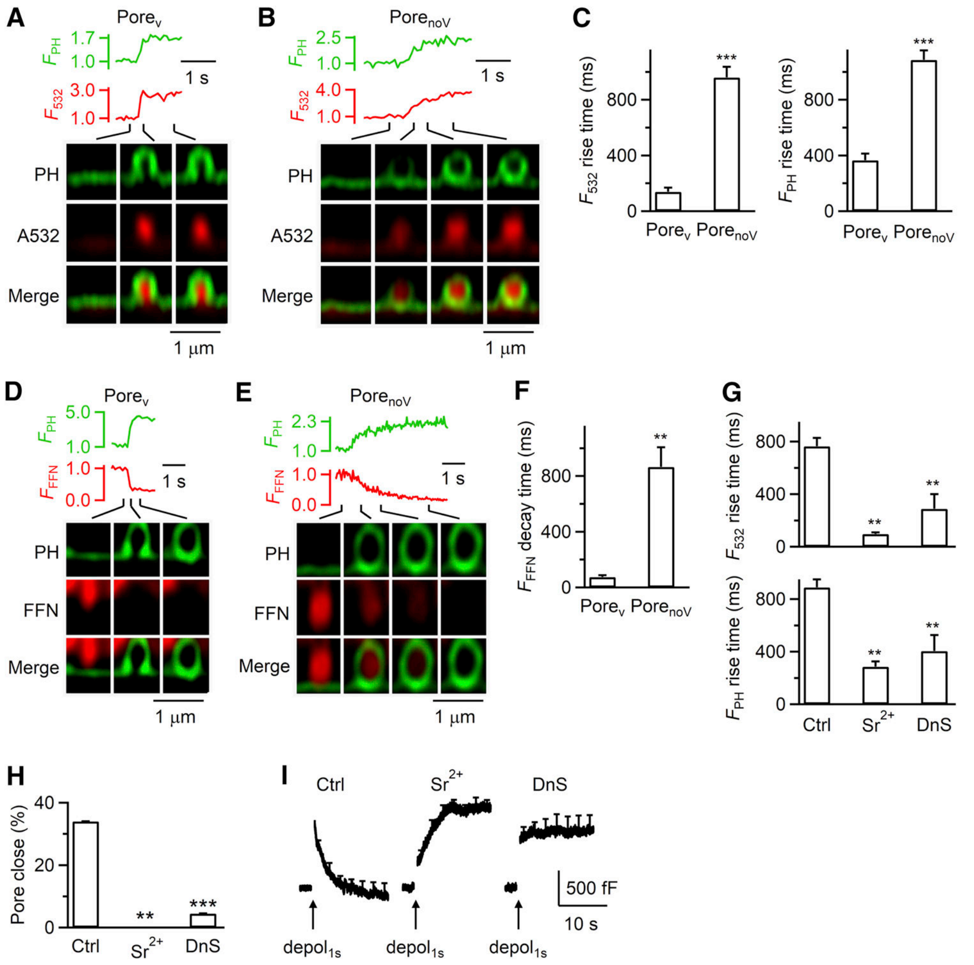

Figure 5. Pore-dynamics control cargo release and endocytosis

(A–B) F_{PH}, F_{532}, and PH_G/A532 images (XZ/Y_{fix}) for depol_{1s}-induced Ω-profiles with Pore_v (A) or Pore_{noV} (B).

(C) 20–80% rise time of F_{532} and F_{PH} for depol_{1s}-induced PH-Ωs with Pore_v (51 Pore_v, 49 cells) or Pore_{noV} (185 Pore_{noV}, 153 cells, XZ/Y_{fix}).

(D–E) F_{PH}, F_{FFN} (FFN511 fluorescence), and PH_G/FFN511 images for depol_{1s}-induced PH-Ω with Pore_v (D) or Pore_{noV} (E).

(F) 20–80% F_{FFN} (FFN511 fluorescence) decay time for PH-Ωs with Pore_v (8 Pore_v, 7 cells) or Pore_{noV} (24 Pore_{noV}, 18 cells).

(G–I) 20–80% rise time of F_{532} and F_{PH} for depol_{1s}-induced PH-Ωs (G), close-fusion percentage (H), and Cm changes induced by depol_{1s} (I) in Ctrl (202 cells) or in the presence of Sr^{2+} (10 cells) or dynasore (DnS, 19 cells, XZ/Y_{fix}).

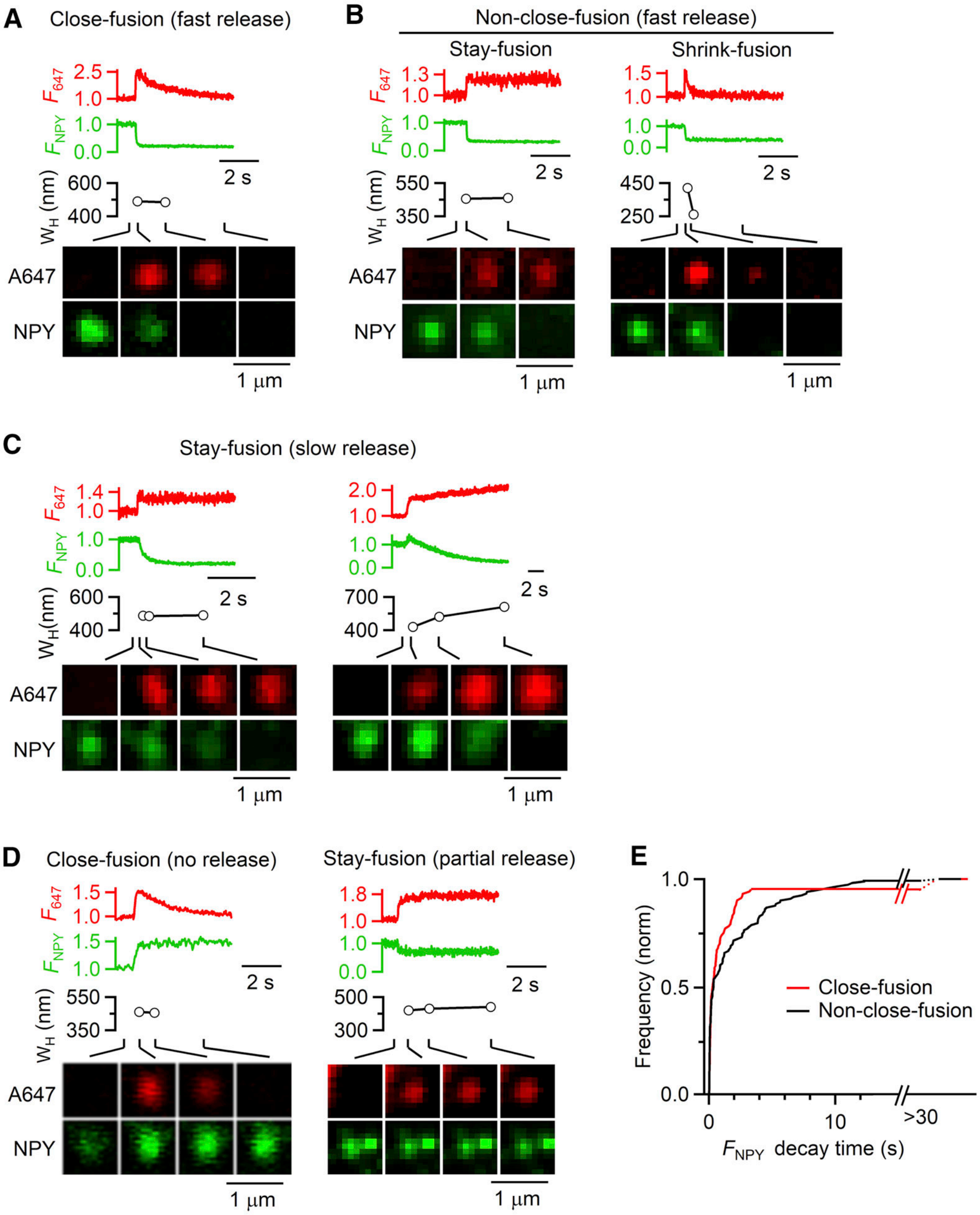

Figure 6. Most close-fusions release NPY-EGFP rapidly and completely as non-close-fusions

(A–D) F_{647} (A647 spot fluorescence), F_{NPY} (NPY-EGFP spot fluorescence), A647 spot W_H, and A647/NPY-EGFP confocal XY-images at times indicated with lines for various fusion modes and rates of releasing NPY-EGFP. A, close-fusion with rapid release; B, non-close-fusion, including stay-fusion (left) and shrink-fusion (right) with rapid release; C, two stay-fusion spots with slow release; D, close-fusion (left) and stay-fusion (right) with no or partial release of NPY-EGFP.

(E) Cumulative frequency (normalized) of 20–80% F_{NPY} decay time for close-fusion (95 spots, 28 cells) and non-close-fusion (123 spots, 28 cells, confocal XY/Z_{fix} imaging). ‘>30 s’: partial or no NPY-EGFP release.